NUMERICAL SIMULATIONS OF A WAVE ENERGY CONVERSION DEVICE USED FOR OCEANOGRAPHIC BUOYS

A Thesis

by

YONGSEOK LEE

Submitted to the Office of Graduate and Professional Studies of
Texas A&M University
in partial fulfillment of the requirements for the degree of

MASTER OF SCIENCE

Chair of Committee,	Jun Zhang
Co-Chair of Committee,	John M. Niedzwecki
Committee Member,	H. Joseph Newton
Head of Department,	Robin Autenrieth

August 2014

Major Subject: Ocean Engineering

ABSTRACT

Moored buoy systems are often deployed by oceanographers to gather scientific information on local and global changes in the water column, weather patterns and climate change. The data they gather is first transmitted to satellites or passing oceanographic ships prior to transmission land based research facilities. Most buoy designs are powered by battery systems that provide ballast and some can be recharged by solar panels. At-sea maintenance may include regular battery replacement or repairs to the buoy system due to vandalism, each being expensive propositions. In order to reduce the costs and utilize green energy, this thesis research investigates the use of incorporating a pendulum wave energy conversion (WEC) device as a permanent or semi-permanent power source for some oceanographic buoys having an average power consumption that can vary from 0.1W to 6.0W.

The main criteria for selecting a WEC device for this application are operational reliability, sustainability during operational and extreme weather conditions, and minimizing the opportunity for vandalism. A general analytical model was developed and simulations of the motions of the buoy were performed using the numerical code COUPLE, which was originally developed to simulate the coupled response behavior of a deepwater floating hull and the associated mooring/riser/tendon systems. Based upon the motion behavior from the numerical simulation, the electrical power output by the selected WEC device is estimated using an iterative scheme to estimate equivalent damping of a hydraulic Power Take-Off (PTO) system.

Several illustrative case studies are presented to verify that the electrical power output rate is in the range of the power demands needed by typical oceanographic buoys. It is concluded that the proposed pendulum WEC device is a feasible solution that can be designed to provide an alternative power system to power oceanographic buoys. The research study provides a way to approach the design and utilization of WEC devices to capture wave energy as a natural power source for a wide range of buoy shapes, sizes and configurations for existing and future buoy designs.

ACKNOWLEDGEMENTS

I would like to express my sincere gratitude to Dr. Jun Zhang, my committee chair, for his continuous encouragement, direction, and inspiration during my study. I also would like to express special thanks to my co-advisor Dr. John M. Niedzwecki for his guidance, motivation, and patience during my research. Sincere thanks are expressed to Dr. H. Joseph Newton for serving as my committee member.

Thanks also go to my colleagues for spending their time with discussion and help. I am also grateful to Dr. Alain H. Clément and Dr. Aurélien Babarit for providing the papers describing the design and principles of SEAREV. My thanks are also expressed to many oceanographers, data buoy operators, and manufacturers for providing data for this research. Finally, thanks to my family for their encouragement and love during my graduate study at Texas A&M University.

NOMENCLATURE

DOF	Degrees-Of-Freedom
FFT	Fast Fourier Transform
HP	High pressure
LP	Low pressure
NOAA	National Oceanic and Atmospheric Administration
PTO	Power Take-Off
WEC	Wave Energy Conversion

TABLE OF CONTENTS

Page

LIST OF FIGURES

Page

LIST OF TABLES

Page

CHAPTER I

INTRODUCTION

1.1 Background

Moored oceanographic buoys measure data obtained in the ocean, such as wind velocity, air and sea surface temperature, salinity, and air pressure, and transmit them to the land through satellite telecommunication systems. These recorded observations make significant contributions to the ability of meteorologists and oceanographers to analyze global weather and climate. The operations performed by buoys consume electricity, and hence batteries are currently used for many oceanographic buoys as their power sources. These batteries usually last a few months or years, and the battery power system bears a high maintenance cost for regular battery replacements. Some of the moored oceanographic buoys utilize solar panels installed on the top of the buoys, but vandalism and stealing of solar panels have been reported (Teng at el., 2009). In order to reduce the maintenance costs and mitigate the risk of losing their power sources, a WEC device is proposed as a permanent or semi-permanent power source for oceanographic buoys.

As tools that use the Eulerian measure, there are many different types of moored oceanographic buoys, which are anchored at fixed locations. Moored buoys have a variety of shapes and sizes depending on their purposes for measurement and conditions under which they are deployed as shown in Fig. 1 that can be found on the webpage provided by National Data Buoy Center (NDBC) of National Oceanic and Atmospheric Administration (NOAA) (NDBC, 2008). Their diameters vary from a few meters to 12

meters (Berteaux, 1991). Among them, 3-meter discus buoys are widely operated by the center since 1983 (Timpe & Teng, 1992).

Knowing the total maximum power requirement for sensors, electronic chips, and transmitters installed on oceanographic buoys is crucial when validating usefulness of renewable power sources, such as WEC. The power requirement will depend on the number and types of sensors, transmission settings, and electrical settings, such as electrical voltages and currents. Using the information given by the operators of moored oceanographic buoys, the average power consumption of a 3-meter discus buoy is surveyed. Based on this power requirement, this research explores the feasibility of using a WEC device as a permanent or semi-permanent energy source in a typical oceanographic buoy through the approach of numerical simulation. If a WEC device can produce enough electrical power, meteorologists and oceanographers may benefit from wave energy as an alternative energy source. Findings through this research investigation can be integrated into the design of oceanographic buoys equipped with the WEC device.

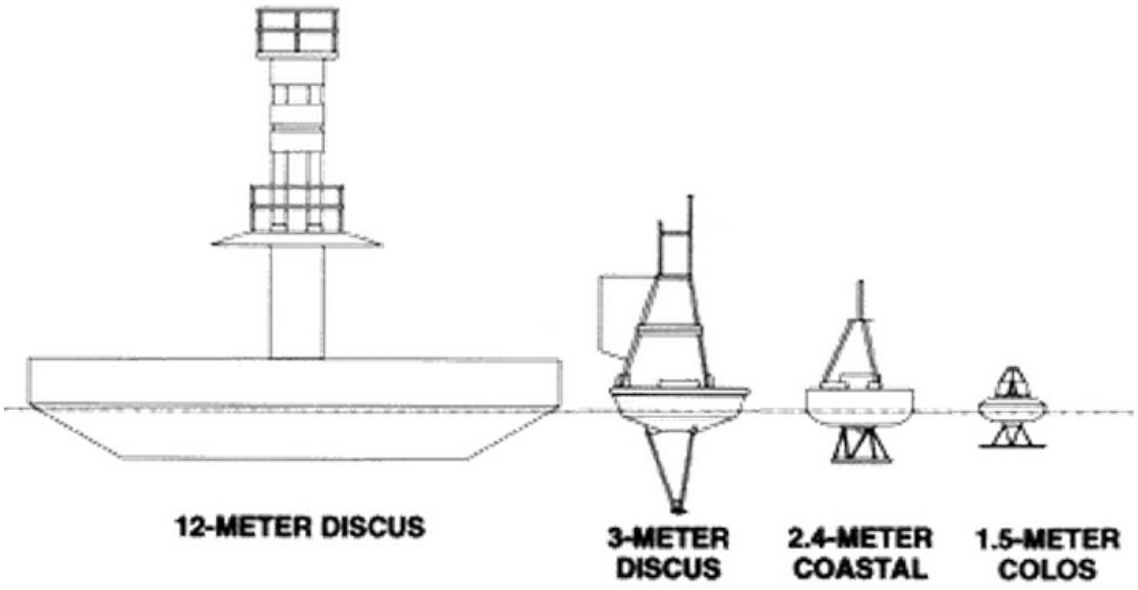

Figure 1 Various types of moored oceanographic buoys (NDBC, 2008)

1.2 Objectives and Research Scope

The following sequential approach is taken in this research investigation. First, an appropriate WEC device concept is selected to be incorporated in the design of a typical disk buoy. The main criteria for choosing the WEC device are reliability, sustainability, and minimizing the opportunity for vandalism and stealing of a power source. Second, a pendulum design model for the relative movement between hull and the Power Take-Off (PTO) system is selected, and then a set of motion equations of the pendulum model is formulated both by a Lagrange's approach and by a Newtonian approach. Third, numerical simulations of the motions of a buoy are made in time domain using COUPLE, which considers actual wave conditions at the locations where a moored buoy is likely deployed. The surge and pitch motions of the floating body excited by regular waves are used as inputs for the pendulum motion to calculate the external moment exciting the motion of the pendulum. Fourth, the work of the hydraulic PTO system is modeled as equivalent damping of the pendulum motion using the concept of the energy transfer from the mechanical energy to electric energy. Finally, an electrical power output by the selected WEC device is estimated through an iterative scheme to accurately estimate the work done by the PTO system. Case studies are conducted to validate the selected WEC device is a feasible solution as a permanent or semi-permanent power source for oceanographic buoys.

CHAPTER II

POWER DEMAND AND WEC DEVICE

2.1 Power Requirement of Oceanographic Buoys

The electric power consumed by sensors, electronic chips, and transmitters of an oceanographic buoy depends on its mission and consequently has a broad range. Typically the power need is provided by batteries, solar panels, or some combination. There are two ways to estimate power consumption. One way is to identify electric power consumptions of each piece of equipment to be deployed on the buoy, and then take the sum of the individual requirement to determine the total power demand. The other way is to inspect the recorded power history using electric current and voltage. Considering the fact that the number and type of sensors are different depending on the buoy mission and where it will be deployed, the average power consumption is calculated through information on the real time electric current uses at its nominal voltage given by operators (Meinig, 2013; Pettigrew & Pigeon, 2013).

In particular, power consumptions highly depend on weather and climate because the transmission of data through a satellite is one of the most consumable elements, and it takes a much longer time with cloudy weather. Considering this fact, the power requirements of buoys are surveyed by selecting a couple of reference buoys which are deployed for different purposes and in different regions (e.g. tropical area and north area). These power consumptions range from 0.1 W to 6.0 W as a daily use because time average electric currents show 12 mA to 0.5 A at nominal 12 voltage.

In addition, marine lanterns attached to the buoy superstructure are normally self-powered independently by small scale solar panels equipped inside of the lantern. However, considering the purpose of this research is to power the entire buoy using wave energy, all components will be included. The power consumption of a marine lantern depends on its uses and factors such as light intensity, eclipse period, and daytime setting. Considering the most typical uses of marine lanterns summarized in Table 1, it can be concluded that the marine lantern requires less than 0.1W, which is insignificant when considering the total power consumption of an instrumental oceanographic buoy.

Table 1 Typical power consumption of a marine lantern

Setting		Value
Light intensity		3 NM
Eclipse period (duty cycle)		10 %
Number of LED		1
Voltage		12 VDC
Current	Night	0.10 A - 0.12A
	Eclipse and daytime	0.9 mA - 1 mA
Daylight time		12 hrs

2.2 Selection of WEC Device

Selecting a suitable WEC device for an oceanographic buoy from existing WEC device concepts considered ease of integration into the buoy design, mechanism simplicity, reliability, and the desire of the minimum maintenance. Thus, the mechanics of SEAREV[1] WEC device was selected as the basis for this study (Babarit, 2005; Babarit et al., 2006). A device similar to SEAREV can be sealed inside the buoy, which avoids the corrosion from the sea water, the attachment of barnacles, and inadvertent damage and minimizes the potential for vandalism. This WEC concept utilizes simple oscillatory motions of an inner pendulum wheel and requires very little maintenance. To avoid corrosion problems, WEC devices that utilized heaving buoys were not chosen although many of their mechanisms are also simple. This is because most heaving WEC devices have moving parts or interfaces, which are between a heaving floater and a reference frame, exposed to sea water as shown Fig. 2.

[1] Système Électrique Autonome de Récupération d'Énergie des Vagues

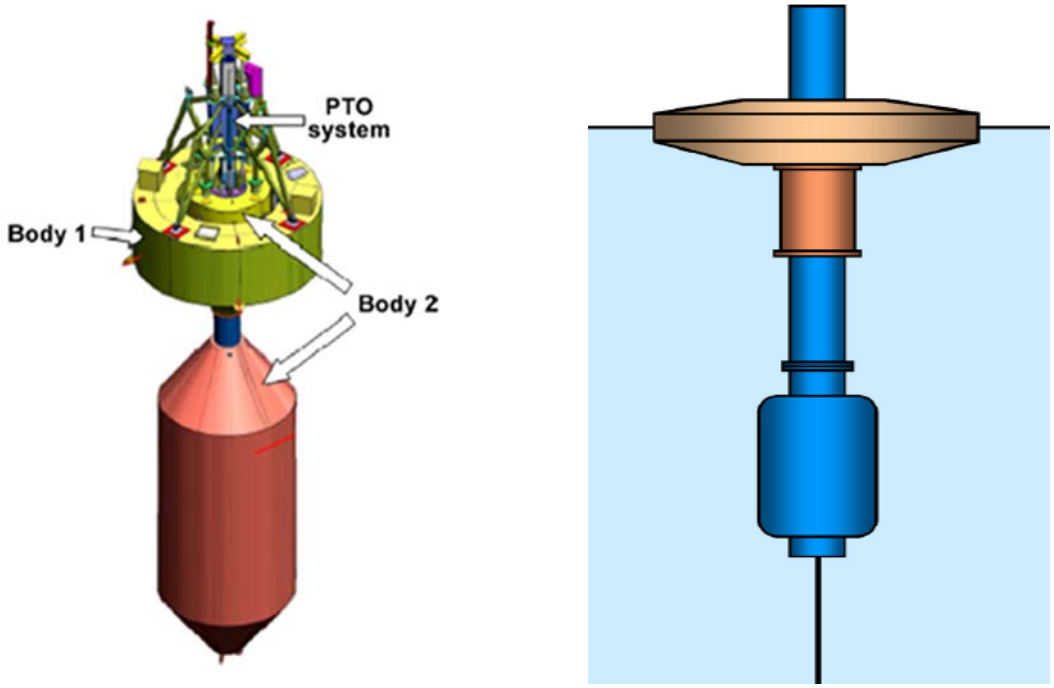

Figure 2 Examples of a heaving buoy: Wavebob (left) and L-10 (right) (Falcao, 2010)

2.3 Principle of WEC Device and Power Take-Off System

The selected WEC device can be envisioned as consisting of a heavy wheel, whose gravitational center is purposely set off from a pivot point, and a Power Take-Off (PTO) system, as shown in Fig. 3. The heavy wheel oscillates about the geometric center at point A when the buoy is experiencing surge, heave, and pitch motions under the impact of ocean waves. The oscillation of the off-centered heavy wheel generates relative motions with respect to the hull of a buoy, which in turn drives the PTO system (e.g. hydraulic system or direct-drive synchronous machine). In Fig. 4, a schematic illustrating the principle of how the PTO system drives a hydraulic motor to generate electricity is presented.

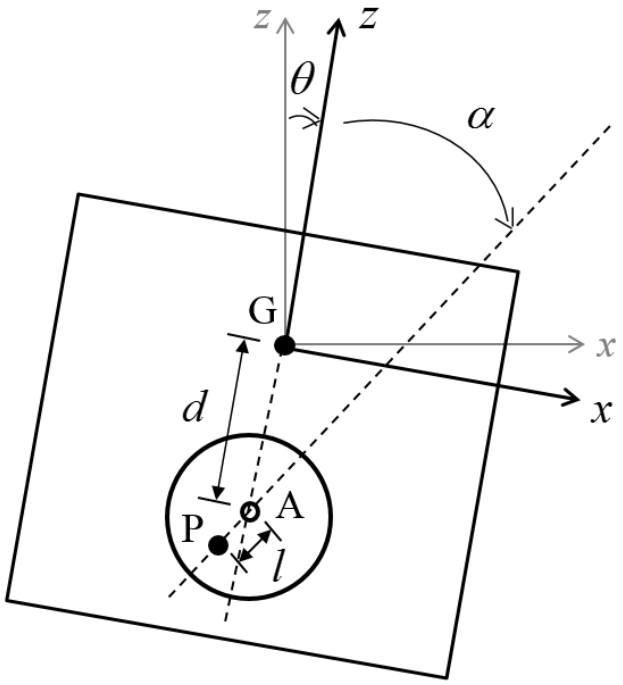

Figure 3 Schematic principle of SEAREV

Previous studies on a SEAREV device include a conceptual PTO with linear damping (Babarit, 2005), a PTO with a hydraulic system (Babarit et al., 2008; Josset et al., 2007), and a PTO with a synchronous machine (Ruellan, et al., 2010). In this research investigation, the PTO with hydraulic system is selected. The hydraulic system package is similar to that of the previous studies on the hydroelectric conversion system of SEAREV. The hydraulic system illustrated in Fig. 4 includes a double acting hydraulic linear ram that is horizontally hinged at the hull, a low pressure (LP) tank, a high pressure (HP) accumulator, and a hydraulic motor and generator. The piston movements (inside of the ram) are induced by the wheel's oscillations. The motion of the piston forces the working fluid to enter the HP accumulator and to leave the LP tank.

The pressure difference between the HP accumulator and the LP tank drives the hydraulic motor, which in turn drives the electric generator (Falcao, 2007).

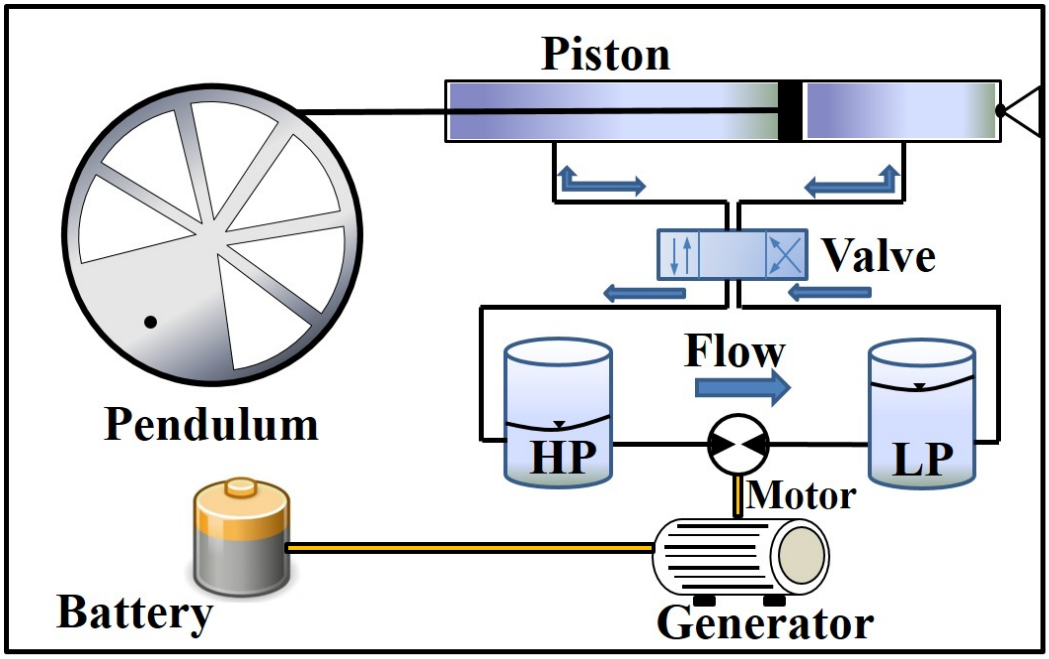

Figure 4 Power Take-Off system for an oceanographic buoy

CHAPTER III

APPROACH AND METHODOLOGY

3.1 Buoy Motion

3.1.1 Coupled Dynamic Analysis and 6-DOF Motion Equation

In this study, the motions of the buoy moored by three mooring lines are simulated in time domain using the numerical code COUPLE, a coupled dynamic analysis program developed by Zhang and his former and currents students at Texas A&M University. A coupled dynamic analysis considers the dynamic interactions between the hull and its mooring lines by including the effect of the time dependent inertia and drag forces of the lines, whereas a conventional quasi-static analysis approach does not consider such effects. Thus, the coupled dynamic analysis provides more reliable results than a quasi-static approach in predicting the motions of floating bodies and tensions in mooring lines (Chen, 2002). In the coupled dynamic analysis, the six Degrees-Of-Freedom (6-DOF) motion equation is properly coupled with its mooring system by matching the displacements and forces at their connection points (fairleads) through hinged boundary conditions. For computing the dynamics of mooring lines, each mooring line is approximated as a slender rod and discretized into many elements, and they are modeled using a finite element method (Garrett, 1982; Ma & Webster, 1994). The space-fixed ($\hat{o}\hat{x}\hat{y}\hat{z}$) and body-fixed ($oxyz$) coordinate systems are employed to calculate the motion of floating bodies as shown in Fig. 5. The governing equations

for the 6-DOF motions of a rigid floating body were derived before (Chen, 2002; Lee, 1995; Paulling & Webster, 1986) and can be expressed as follows.

$$m\frac{d^2\xi}{dt^2}+m\mathbf{T}^{\mathbf{t}}\left(\frac{d\boldsymbol{\omega}}{dt}\times\mathbf{r}_{\mathbf{g}}\right)+m\mathbf{T}^{\mathbf{t}}\left(\boldsymbol{\omega}\times\left(\boldsymbol{\omega}\times\mathbf{r}_{\mathbf{g}}\right)\right)=\hat{\mathbf{F}} \tag{1}$$

$$\mathbf{I}_o\frac{d\boldsymbol{\omega}}{dt}+\boldsymbol{\omega}\times\mathbf{I}_o\boldsymbol{\omega}+m\mathbf{r}_{\mathbf{g}}\times\left(\mathbf{T}\frac{d^2\xi}{dt^2}\right)=\mathbf{M}_o \tag{2}$$

where, $\boldsymbol{\xi}=(\xi_1, \xi_2, \xi_3)^T$ is the coordinate of the point o in the space-fixed coordinate, the **T** is the transfer matrix between the body-fixed and space-fixed coordinate system, the superscript **t** indicates the transpose of a matrix, $\boldsymbol{\omega}=(\omega_1, \omega_2, \omega_3)^T$ is the angular velocity, $\mathbf{r}_g=(x_g, y_g, z_g)^T$ is the vector of the center of gravity, $\mathbf{I}_o$ is the moment of inertia of the body, and $\hat{\mathbf{F}}$ and $\mathbf{M}_o$ represent the total forces and the total moments applied on the rigid body respectively. Note that $\boldsymbol{\omega}$, $\mathbf{r}_g$, $\mathbf{I}_o$, and $\mathbf{M}_o$ are expressed with respect to the body-fixed coordinate. Euler angles and their sequence related roll, pitch, yaw are detailed in Appendix A.

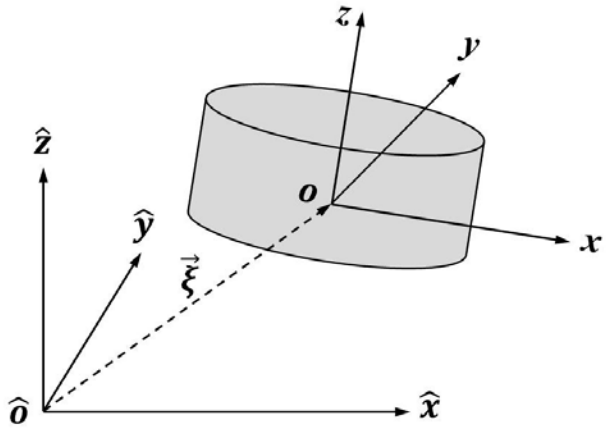

Figure 5 Coordinate system for a rigid slender body

3.1.2 Morison Equation for Wave Loads

Wave loads applied on a floating body include radiation and diffraction wave loads in addition to incident wave loads. The radiation and diffraction wave loads can be critical when a floating body has large horizontal dimensions in comparison with the wavelength of the incident wave. The radiation waves are generated by the motions of the floating body, which consumes the energy, is known as radiation damping. However, considering the size of oceanographic buoys (4-m diameter) and typical wavelengths of waves considered in this study (from 25 m to rough 100 m), the slender body approximation is a reasonable approximation for this study.

Thus, Morison Equation can be employed, and consequently the radiation and diffraction wave loads are neglected. This approach simplifies the calculation and provides an accurate estimate of wave loads provided that the ratio of wavelength to the diameter of a slender body $\lambda/D>5$ (Faltinsen, 1990). Because of these merits, Morison Equation is widely used to calculate wave loads on slender floating structures (Ahmad, 1996; Henderson & Patel, 1998; Jain, 1997).

Recently, COUPLE has been updated for shallow draft floating body's simulations (Zhang, 2014). In particular, COUPLE considers wave slopes when calculating bottom pressure applied on the floating body. The consideration may change external moments for wave loads. This is critical in order to have accurate results for pitch motions and coupled surge motions of all kind of shallow draft bodies such as oceanographic buoys or CALM (Catenary Anchor Leg Mooring) buoys used in the oil

and gas industry. As long as the motions (mainly surge and pitch) of the moored buoy are accurately estimated, the power by the PTO can also be estimated accurately.

In addition, using the nonlinear deterministic Hybrid Wave Model (HWM), COUPLE has the following uniqueness and advantage. The wave kinematics are predicted up to the free surface and at least accurate up to second order in wave steepness (Jia, 2012; Spell et al., 1996; Zhang et al. 1996). Thus, there is no necessity for choosing an estimation among several empirical or stretching approximations, such as linear extrapolation and wheeler stretching.

3.2 Pendulum Oscillation

3.2.1 Pendulum Model

The SEAREV WEC device is modeled as a pendulum model that captures the interaction between the hull and its PTO system as shown in Fig. 6. As in an earlier study by Babarit (2005), the motion of the buoy is assumed to be two dimensional. Thus, this pendulum model has 4 Degrees-Of-Freedom (DOF), the surge, heave, and pitch of the buoy, and the relative motion (angle) between the hull and the wheel. The model is similar to the model shown in the previous study, but the difference between them is that the point G in Fig. 6 represents the center of gravity of the entire buoy in Fig. 3 including the inner pendulum wheel in addition to its hull.

The pendulum system experiences a damping force by taking the hydraulic PTO system into account. This damping causes reduction in the amplitude of oscillation of the pendulum P in Fig. 6. The damped oscillation of the wheel P is accurately calculated

using equivalent damping and an iterative scheme in later sections. Once the motions of the buoy are accurately calculated, the damped oscillation of the pendulum P can also be estimated accurately.

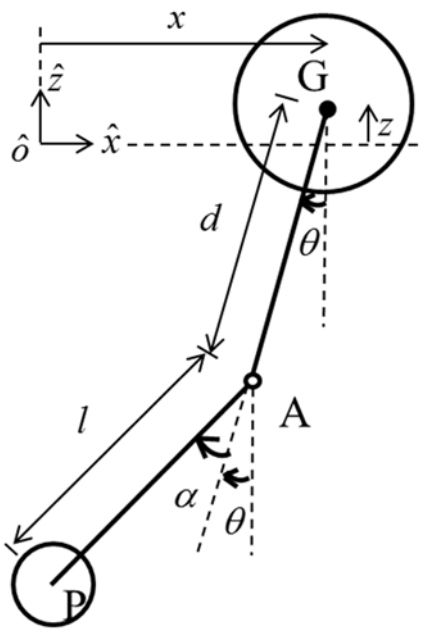

Figure 6 Pendulum model of SEAREV

3.2.2 Pendulum Motion Equation Derived using a Langrange's Approach

The oscillation of the pendulum shown in Fig. 6 is forced by the surge, heave, and pitch motions of the buoy (shown as G wheel in the figure), which can be calculated using COUPLE. One approach to formulate the equation of motion for the pendulum model is to use a Lagrange's approach.

Let L be the Lagrangian quantifying kinetic energy and potential energy expressed in terms of generalized variables. The Lagrange's approach is based on the concept that the sum of kinetic energy and potential energy is constant in a conservative system (Baruh, 1999; Thomson, 1972).

$$L = K - P \tag{3}$$

where, K is total kinetic energy, and P is total potential energy.

$$\frac{d}{dt}\left(\frac{\partial L}{\partial \dot{q}_i}\right) - \frac{\partial L}{\partial q_i} = 0, \qquad i = 1, 2, ..., M \tag{4}$$

where, q_i and $\dot{q}_i$ are generalized variable and velocity respectively, and M is the number of generalized variables involved in L. In order to define L, the coordinates of point G and P must be defined.

$$\begin{aligned} G &= (x, z) \\ P &= \left(x - d\sin\theta - l\sin(\theta + \alpha),\ z - d\cos\theta - l\cos(\theta + \alpha)\right) \end{aligned} \tag{5}$$

where, x, z, and θ are surge, heave, pitch of the floating body, and α is the relative angle between the hull and the pendulum wheel. d is the distance from the center of gravity of the floating body, G, to the pivot point of the wheel A, and l is the distance from the pivot point to the mass center of the pendulum wheel.

It follows then that the Lagrangian L can be expressed as

$$
\begin{aligned}
L \;&= \frac{1}{2}\left(m_1+m_2\right)\dot{x}^2 + \frac{1}{2}I_1\dot{\theta}^2 + \frac{1}{2}I_2\left(\dot{\theta}+\dot{\alpha}\right)^2 \\
&\quad + \frac{1}{2}m_2\left[\begin{array}{l} d^2\dot{\theta}^2 + l^2\left(\dot{\theta}+\dot{\alpha}\right)^2 \\ +2\left\{-d\,\dot{x}\,\dot{\theta}\cos\theta - l\,\dot{x}\left(\dot{\theta}+\dot{\alpha}\right)\cos\left(\theta+\alpha\right) + d\,l\,\dot{\theta}\left(\dot{\theta}+\dot{\alpha}\right)\cos\alpha\right\}\end{array}\right] \\
&\quad + m_2 g\left\{d\cos\theta + l\cos\left(\theta+\alpha\right)\right\}
\end{aligned}
\tag{6}
$$

where, m_1, m_2, I_1, and I_2 are the mass and moment of inertia of the buoy hull and pendulum wheel respectively, and g the gravitational acceleration.

Then it follows from the application of Eq. 4 that a system of non-linear motion equations results. The resulting equation for these two pendulums in the conservative system can be written in the matrix form

$$
M\ddot{X} + F_P = 0 \tag{7}
$$

where, M is mass matrix, X is the set of generalized variables, F_p is pendulum matrix for the remaining terms including gravitational forces.

$$
X = \left(x,\, z,\, \theta,\, \alpha\right)^T, \tag{8}
$$

$$
M = \left(\begin{array}{cc}
m_1+m_2 & 0 \\
0 & m_1+m_2 \\
-m_2\,d\cos\theta - m_2\,l\cos\left(\theta+\alpha\right) & m_2\,d\sin\theta + m_2\,l\sin\left(\theta+\alpha\right) \\
-m_2\,l\cos\left(\theta+\alpha\right) & m_2\,l\sin\left(\theta+\alpha\right)
\end{array}\right.
\left.\begin{array}{cc}
-m_2\,d\cos\theta - m_2\,l\cos\left(\theta+\alpha\right) & -m_2\,l\cos\left(\theta+\alpha\right) \\
m_2\,d\sin\theta + m_2\,l\sin\left(\theta+\alpha\right) & m_2\,l\sin\left(\theta+\alpha\right) \\
I_1+I_2+m_2\,d^2+m_2\,l^2+2m_2\,d\,l\cos\alpha & I_2+m_2\,l^2+m_2\,d\,l\cos\alpha \\
I_2+m_2\,l^2+m_2\,d\,l\cos\alpha & I_2+m_2\,l^2
\end{array}\right), \tag{9}
$$

$$F_P = \begin{pmatrix} m_2 d\dot{\theta}^2 \sin\theta + m_2 l\left(\dot{\theta}+\dot{\alpha}\right)^2 \sin\left(\theta+\alpha\right) \\ \left(m_1+m_2\right)g + m_2 d\cos\theta\cdot\dot{\theta}^2 + m_2 l\cos\left(\theta+\alpha\right)\cdot\left(\dot{\theta}+\dot{\alpha}\right)^2 \\ -m_2 d l\left(2\dot{\theta}\dot{\alpha}+\dot{\alpha}^2\right)\sin\alpha + m_2 g\left\{d\sin\theta + l\sin\left(\theta+\alpha\right)\right\} \\ m_2 d l\dot{\theta}^2 \sin\alpha + m_2 g l\sin\left(\theta+\alpha\right) \end{pmatrix}. \tag{10}$$

The details of the derivation are shown in Appendix B.

The fourth row in vector *X* is the generalized variable *α,* and the related equation governs the motion of the inner pendulum wheel. The equation is linearized by assuming both pitch angle θ and the relative angle α are small, as shown in Eq. 11 and Eq. 12 given below. It should be noted that heave acceleration is much smaller than gravitation acceleration in case simulations, so nonlinear terms which have the heave acceleration are neglected. Besides, as the configuration of the PTO implies, heave acceleration at small pitch angles cannot make significant contribution to pendulum motions. Thus, heave acceleration is neglected for power generation, although COUPLE calculates all of 6-DOF buoy motions including heave motions.

$$\left(I_2 + m_2 l^2\right)\ddot{\alpha} + m_2 g l\alpha = M\left(t\right) \tag{11}$$

$$M\left(t\right) = m_2 l\,\ddot{x} - \left(I_2 + m_2 l^2 + m_2 dl\right)\ddot{\theta} - m_2 g l\theta \tag{12}$$

where, *M(t)* is the forcing term, resulting from motions of the buoy.

M(t) is contributed from kinetic energy and potential energy induced by surge and pitch motions, that is, their accelerations. Thus, the forcing term *M(t)* is divided into two parts, related to surge and pitch, respectively as shown in Eq. 13 and Eq. 14.

$$M_{\text{surge}}\left(t\right) = m_2 l\,\ddot{x} \tag{13}$$

$$M_{\text{pitch}}(t) = -\left(I_2 + m_2 l^2 + m_2 dl\right)\ddot{\theta} - m_2 gl\theta \tag{14}$$

The given motions induced by regular waves are approximated by sinusoidal functions, and these forcing terms are used for estimating responses of the pendulum's oscillation respectively.

The motion equation for this pendulum model derived here is identical with the motion equations derived using a free body diagram and vector mechanics in the earlier study by Babarit (2005), by correcting the typo *–d* to *d*. The system of linearized motion equations for $X=(x, z, \theta, \alpha)^T$ by the Lagrange's approach is given in Appendix B.

3.2.3 Pendulum Motion Equation Derived using a Newtonian Approach

The pendulum motion derived by the Lagrange's approach can also be derived using a Newtonian approach. The following free-body diagram depicts the all forces and moments applied on the pendulum wheel.

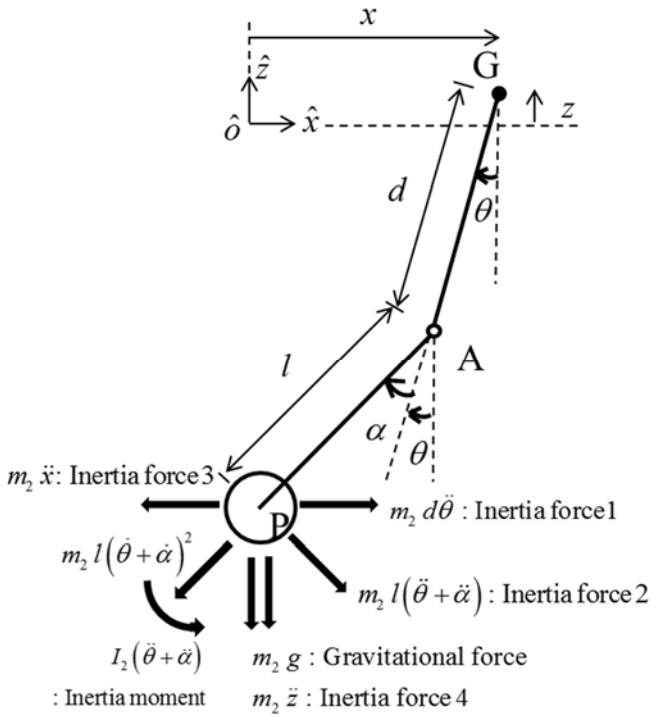

Figure 7 Free-body diagram for the pendulum motion

where, the inertia force 1 is due to pitch of the floating body, and the inertia force 2 and inertia moment due to rotational motions of inner wheel with respect to the point A. The mass moment of inertia is the centroidal mass moment of inertia of the pendulum wheel. The inertia force 3 results from the surge acceleration of the body, and inertia force 4 is from the heave acceleration.

Some of forces related to moments about the axis through A is analyzed by following vector mechanics.

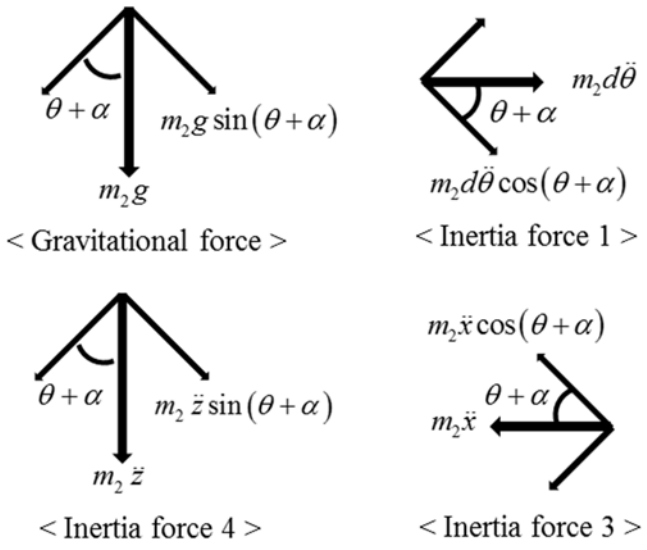

Figure 8 Vectors for applied forces

Moment equilibrium with respect to A provides the following equation, which is consistent with the motion equation derived through the energy based approach in the previous section.

$$\sum M_A = \left(I_2 + m_2 l^2\right)\left(\ddot{\theta}+\ddot{\alpha}\right) + m_2 g l\sin\left(\theta+\alpha\right) + m_2 d l\ddot{\theta}\cos\left(\theta+\alpha\right) - m_2 l\ddot{x}\cos\left(\theta+\alpha\right) + m_2 l\ddot{z}\sin\left(\theta+\alpha\right) = 0 \tag{15}$$

In the next section, the subscripts "2" have been removed. That is I refers I_2 and m refers m_2.

3.3 Estimation of Electric Power Generation

The motion equations derived using the Lagrange approach do not involve the damping resulting from the energy transfer from the mechanical energy to electric energy. Thus, this section presents an iterative scheme to estimate equivalent damping

coefficient, quantifying work done during the gas (or hydraulic oil) compression by the ram in the HP accumulator. Using this scheme, not only the damping due to energy transfer is considered, but also the produced electrical power is accurately estimated. For simplification, the pressure difference between two chambers of the double acting cylinder is assumed as constant. The work, *W,* done in a wave period, *T*, is

$$W = \int_0^T \Delta p \cdot S \cdot \left| \dot{X}_p \right| \, dt \tag{16}$$

where, Δp is the pressure difference between the HP accumulator and the LP tank, S is the piston area, and $\dot{X}_p$ is the velocity of the piston. Since the work done by the piston consumes the energy of the oscillating wheel, the energy dissipation of the oscillating wheel during one wave period should be equal to the work done by the ram. The dissipated energy of the oscillating wheel, E, is calculated by evaluating the integral

$$E = \int_0^T b\dot{X}_p \cdot \dot{X}_p \, dt \tag{17}$$

where, b is the damping coefficient obtained by equating Eq. 16 and Eq. 17. This equivalent damping is considered in motion equation of the wheel.

The displacement of the piston is related to the rotational angle through the coefficient λ. For this coefficient, the half of the distance between two end points (back and forth) of the piston during one cycle of oscillation divided by the amplitude of relative angle is taken.

$$X_p = \lambda \alpha \tag{18}$$

After considering the damping, Eq. 11 can be modified and expressed as

$$\left(I + ml^2\right)\ddot{\alpha}_{n+1} + b_n\lambda_n{}^2\dot{\alpha}_{n+1} + mgl\alpha_{n+1} = M_{\text{surge or pitch}}\left(t\right) \tag{19}$$

where, the subscript *n* indicates the number of iterations and the right-hand side (RHS) represents a forcing term, either Eq. 13 or Eq. 14.

The iteration converges quickly after a few iterations. Finally, the produced electrical energy is estimated by Eq. 20 for surge and pitch separately, and then the summation of each power output is applied to estimate the total power output. The equivalent damping *b* retains the amplitude of oscillation at the previous iteration as an element. Thus, in order to conservatively estimate the total power output, the summation of each power output from $M(t)_{\text{pitch}}$ and $M(t)_{\text{surge}}$ is applied and replaces $M(t)$ in Eq. 12.

$$P = \frac{1}{T}\int_0^T \Delta p \cdot S \cdot \left|\dot{X}_{p,\, i=N}\right| dt \tag{20}$$

where, *N* is the last iteration number.

The non-dimensional damping ratio can be expressed as

$$\zeta = \frac{b_{i=N} \cdot \lambda_{i=N}{}^2}{2\sqrt{mgl \cdot \left(I + ml^2\right)}} \tag{21}$$

By applying the iteration scheme at each pressure condition, the optimum electrical power and the pressure condition can be calculated.

CHAPTER IV

NUMERICAL SIMULATION

4.1 Simulation Particulars

4.1.1 Selection of Wave Conditions

The wave conditions used in the numerical simulations were selected from data in the Gulf of Mexico and are for relatively benign sea conditions. The wave conditions at a water depth of 80 m are based on actual records by a NOAA buoy at Station 42020, which is deployed in the sea near Corpus Christi in Texas, and represents the benign sea states of the Gulf of Mexico. The significant wave height and wave dominant period, which is the period with the maximum wave energy, for 5 years (from 2008 to 2012) are presented in Table 2. The data range for significant wave height is from 0.00m to 8.25m, and the range for peak period is from 0.5 sec to 15.5 sec. Data beyond these ranges is not considered. The original data set provided by NOAA can be found on their webpage (NDBC, 2013).

Table 2 Wave data recorded by a NOAA buoy at Station 42020 in the Gulf of Mexico

\Tp(sec) Hs(m)	0.5 -1.5	1.5 -2.5	2.5 -3.5	3.5 -4.5	4.5 -5.5	5.5 -6.5	6.5 -7.5	7.5 -8.5	8.5 -9.5	9.5 -10.5	10.5 -11.5	11.5 -12.5	12.5 -13.5	13.5 -14.5	14.5 -15.5	Sum	%
0.0-0.25	0	0	0	0	0	0	0	0	0	0	0	0	0	0	0	0	0.00
0.25-0.75	0	8	1001	1775	2387	1782	826	398	62	36	11	3	3	1	0	8293	19.65
0.75-1.25	0	0	93	1567	3226	4970	2868	1150	191	59	23	0	4	1	0	14152	33.53
1.25-1.75	0	0	0	72	1005	3181	3331	1619	221	70	4	3	4	4	0	9514	22.54
1.75-2.25	0	0	0	2	90	1154	2317	1800	302	89	13	1	6	8	0	5782	13.70
2.25-2.75	0	0	0	0	8	243	885	1200	222	59	9	0	3	10	0	2639	6.25
2.75-3.25	0	0	0	0	0	20	251	618	176	34	13	0	3	5	0	1120	2.65
3.25-3.75	0	0	0	0	0	2	50	247	85	33	16	0	11	3	0	447	1.06
3.75-4.25	0	0	0	0	0	0	7	74	32	21	7	0	7	9	0	157	0.37
4.25-4.75	0	0	0	0	0	0	0	12	13	10	5	0	1	2	0	43	0.10
4.75-5.25	0	0	0	0	0	0	0	3	5	8	5	0	1	0	0	22	0.05
5.25-5.75	0	0	0	0	0	0	0	0	0	3	3	0	0	4	0	10	0.02
5.75-6.25	0	0	0	0	0	0	0	0	1	2	4	0	2	1	0	10	0.02
6.25-6.75	0	0	0	0	0	0	0	0	0	1	2	0	1	1	0	5	0.01
6.75-7.25	0	0	0	0	0	0	0	0	0	0	2	0	1	0	0	3	0.01
7.25-7.75	0	0	0	0	0	0	0	0	0	2	2	0	0	0	0	4	0.01
7.75-8.25	0	0	0	0	0	0	0	0	0	0	0	0	0	0	0	0	0.00
Sum	0	8	1094	3416	6716	11352	10535	7121	1310	427	119	7	47	49	0	42201	100.00
%	0.00	0.02	2.59	8.09	15.91	26.90	24.96	16.87	3.10	1.01	0.28	0.02	0.11	0.12	0.00	100.00	

Based on Table 2, ten different wave conditions were chosen to represent the yearly local wave conditions, and these are summarized in Table 3. The percentages indicate the probability of the occurrence for the related wave conditions in a one year-timeframe.

Table 3 Computational domain

Water Depth	T_p	H_s	Probability
79.9m	4.0 sec	0.5 m	6.4%
	5.0 sec	0.5 m	8.7%
		1.0 m	11.6%
	6.0 sec	0.5 m	6.4%
		1.0 m	17.9%
		1.5 m	11.5%
	7.0 sec	1.0 m	10.4%
		1.5 m	12.1%
		2.0 m	8.4%
	8.0 sec	2.0 m	6.6%

4.1.2 Selection of the Buoy and Mooring System

A 3-meter discus buoy is commonly used by NOAA. The height of the buoys' hull is in the range of 1 to 2 meters, and they weigh between 0.8 to 3.2 tons in the absence of any payloads. Based on the estimates of the size of the oscillating wheel needed to generate the desired electric power, two oceanographic buoys with cylindrical shapes (WEC-1 and WEC-2) were chosen for this research study. Originally a discus buoy of 3-meters in diameter was considered, but the dimensions were increased considering the size of the wheel and the PTO system needed to generate enough electrical power. Table 4 lists the sizes of WEC-1 and WEC-2 and the dimensions of the

PTO systems. The arrangement of mooring system attached to the buoy is sketched in Fig. 9. The overlooking view of the mooring system is also sketched in the figure, and the properties of the mooring system are summarized in Table 5.

The shape of the pendulum is composite with a rectangular body and a fan-shape body as shown in Fig. 10. In order to make *l* large, the fan-shape is considered, and the rectangular body, whose length is same as the radius of the fan-shape and width is small, is considered only for attaching a piston rod. Attaching concentrated mass near the edge of the pendulum is helpful in making *l* larger, as previous studies on SEAREV did (Ruellan et al., 2010). It is expected that the concentrated mass helps to generate larger electric power with the smaller mass of pendulum because of the relatively larger *l*. However, considering the limited space inside of the buoy due to arrangements of additional equipment, such as an accumulator and hydraulic motor, the solid homogeneous fan-shape is considered, which reduces maximum thickness of the wheel. The sensitivity of the pendulum wheel thickness is discussed in Appendix C.

The horizontal attachment of the hydraulic cylinder to the hull is different from the previous study by Josset et al (2007) and reflects the limited space inside of the oceanographic buoy. The limited length of the hydraulic piston obstructs a full revolution of the wheel as shown in Fig. 10. The related problem caused by the limited stroke can be solved in two ways. First, the pendulum is set to be mechanically disconnected from the hydraulic cylinder beyond a certain angles such as ±30° for WEC-2. Second, attaching blocks between both the hull and the pendulum makes oscillations stop at the limited angle.

Table 4 Dimensions of WEC devices

	Dimensions		Unit	WEC-1	WEC-2
Buoy Hull	Diameter		m	4	
	Height		m	2.5	
	Draft		m	0.65	
	Mass		kg	4,000	
	C.G.		m	1.36	
	C_m		-	1.0	
	C_d		-	1.0	
Inner Wheel	Mass		kg	1,000	
	Diameter		m	1.3	2.0
	d		m	-	-
	l		m	0.306	0.470
	Width of rectangular part		cm	6.5	10.0
	Angle of fan-shape		°	107.1	107.1
	Moment of inertia		$kg \cdot m^2$	111.1	263.1
	Thickness	Steel	cm	29.2	12.3
		Concrete	cm	99.5	42.0
Piston	Diameter of cylinder		cm	5.0	
	Length of piston rod		m	1.20	
	Pressure difference		bar	0.01 – 3.00	

where, C.G. in the table is the center of gravity for buoy hull including inner wheel. C_m is the added-mass coefficient for the circular cylinder. The moment of inertia in the table is the centroidal mass moment of inertia of the inner pendulum.

Table 5 Specification of the mooring system

Dimensions	Unit	WEC-1	WEC-2
Number of mooring lines	ea	3	
Length of mooring lines	m	500	
Mass per unit length in air	kg/m	6.50	
Elastic stiffness (EA)	N	2.89e07	
Pretension	N	1.63e04	

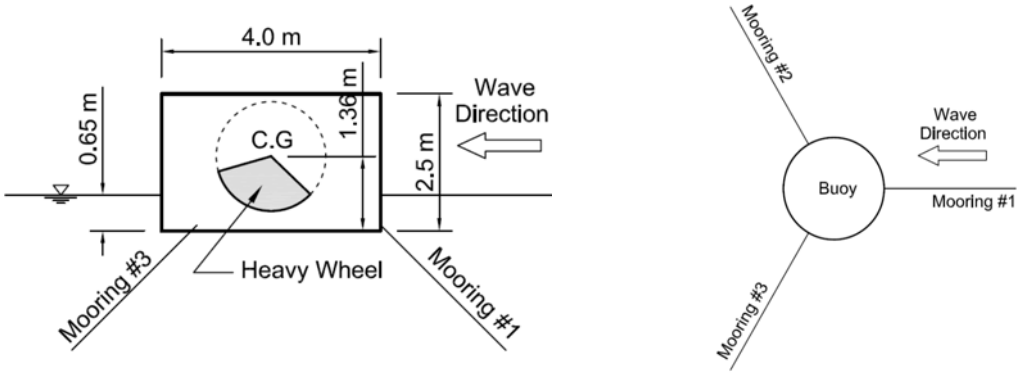

Figure 9 Sketch of the buoy and mooring system

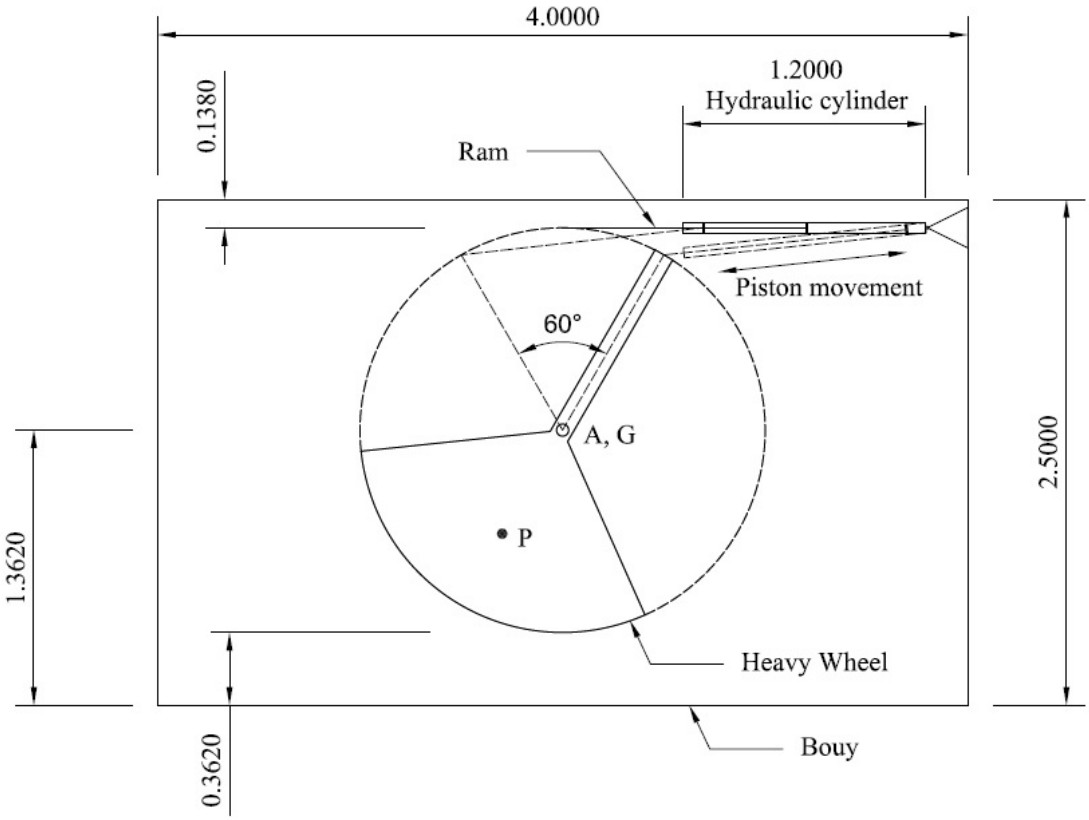

Figure 10 Arrangement of the inner pendulum wheel (WEC-2) with dimensions in the unit of meter

4.2 Buoy Motions

Numerical simulations for 6-DOF motions of the buoy excited by regular waves are made using the numerical code COUPLE. The surge and pitch motions for the most probable site wave condition (H= 1.0 m, T= 6.0 sec) are presented in Fig. 11 and Fig. 12. Other results for the other nine wave conditions are presented in Appendix D. The amplitude of the motions of all ten wave conditions are tabulated in Table 6. To be

specific, this amplitude is measured based on peak to trough values of one regular motion in the range of 450 sec to 500 sec, when the related motions reach steady state.

It was assumed that motions are sinusoidal, and this approach was used for computing external moment, *M(t)*, used in Eq. 13 and Eq. 14. Many of time series results approximate a sinusoidal function, but some of pitch motions show highly nonlinearity (e.g. H=1.0 m, T=5.0 sec and H=2.0 m, T=8.0 sec). Thus, to estimate an electric power output conservatively, FFT (Fast Fourier Transform) is used to obtain the first harmonic data from the simulation results neglecting the second and higher harmonics. This is because the amplitude of the first harmonic data is usually smaller than the amplitude of original simulation data for surge and pitch. The amplitudes of the first harmonic data are also listed in Table 6. Both amplitudes (a half of peak to trough value and the first harmonic by FFT) are used and compared for simulating the electric power output discussed in later sections.

In this frequency range, the results show that the shorter the wave periods and the higher the wave heights, the larger the surge and pitch motions. Furthermore, wave height is more important than wave period to have larger surge and pitch, which is expected.

Also, as discussed in the previous chapter, wave slopes are considered for calculating bottom pressures applied to the oceanographic buoy which has a shallow daft. To be specific, surge and pitch motions are reduced by an average 17% and 64% respectively for the ten regular wave cases considered in this study. In this thesis, only the results with the consideration of wave slope are shown and discussed.

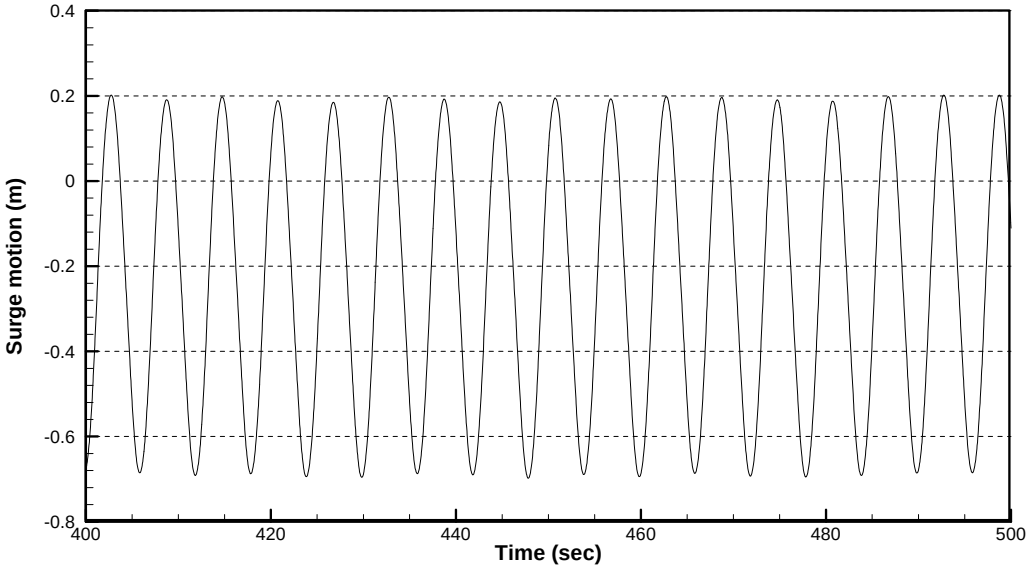

Figure 11 Surge motion for one regular wave case (H=1.0 m, T=6.0 sec)

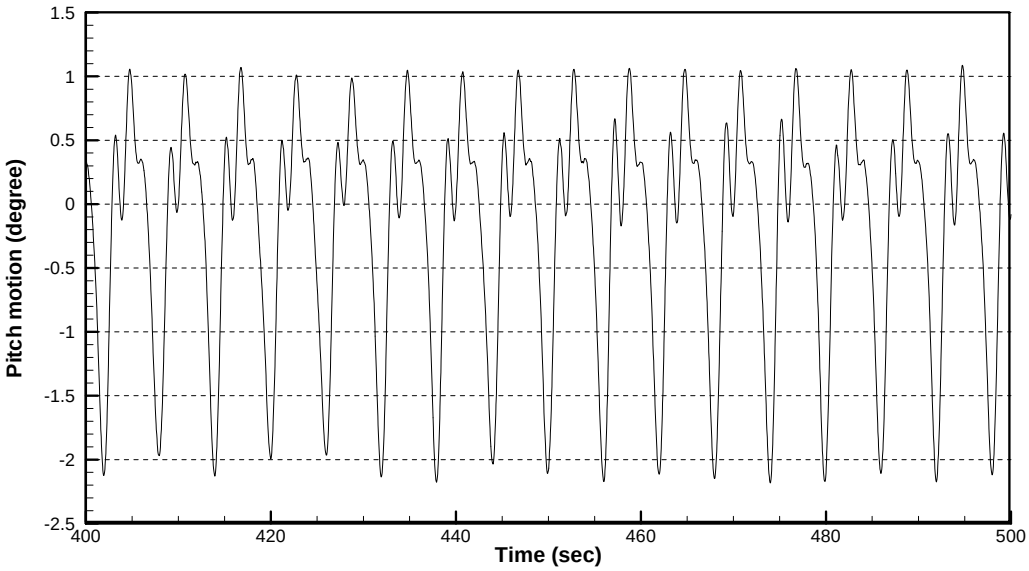

Figure 12 Pitch motion for one regular wave case (H=1.0 m, T=6.0 sec)

Table 6 Floating body motions calculated by COUPLE

T [sec]	H [m]	Amplitude			
		A half of peak to trough value		FFT	
		Surge [m]	Pitch [°]	Surge [m]	Pitch [°]
4	0.5	0.230	1.440	0.231	1.259
5	0.5	0.240	0.750	0.224	0.567
	1.0	0.460	2.500	0.423	1.559
6	0.5	0.248	0.500	0.205	0.303
	1.0	0.450	1.600	0.366	0.900
	1.5	0.625	3.025	0.528	1.613
7	1.0	0.465	1.010	0.338	0.483
	1.5	0.590	1.600	0.429	0.905
	2.0	0.750	2.550	0.541	1.333
8	2.0	0.700	2.600	0.707	1.346

4.3 Power Output

4.3.1 Power Output from Regular Waves

Based on the surge and pitch motions, the related power output is estimated for each given regular wave. This section presents the results for power estimation for the most occurring wave condition (H=1.0m, T=6.0 sec). Figs. 13-16 shows iteration results at 0.2 bar of the pressure difference (Δp) between the HP accumulator and the LP tank.

The figures confirm that the estimated power output, damping ratio, and response of the pendulum motion converge quickly for both WEC configurations. To be specific, it takes at most about 5-7 iterations to reach the convergence. In the case of surge, it takes only 2-3 iterations, and the changes are relatively smaller than the cases of pitch. This is because $M(t)_{\text{surge}}$ is much larger than $M(t)_{\text{pitch}}$, so the damping corresponding to 0.2 bar (Δp) is a relatively larger resistance for pendulum motions induced by pitch motions than by surge motions.

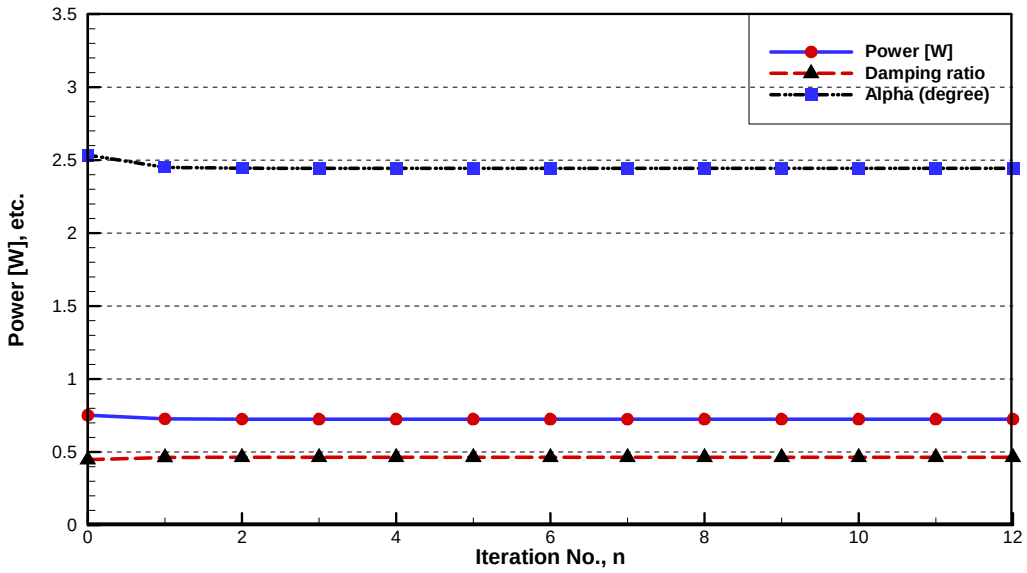

Figure 13 Convergence at Δp = 0.2 bar for one regular wave case (H=1.0 m, T=6.0 sec) using WEC-1 (surge only)

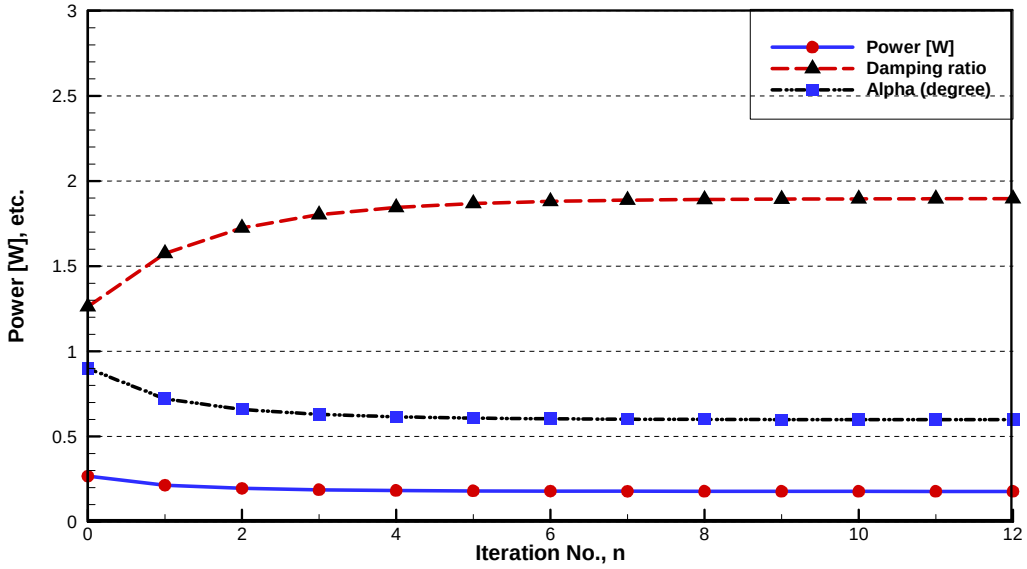

Figure 14 Convergence at Δp = 0.2 bar for one regular wave case (H=1.0 m, T=6.0 sec) using WEC-1 (pitch only)

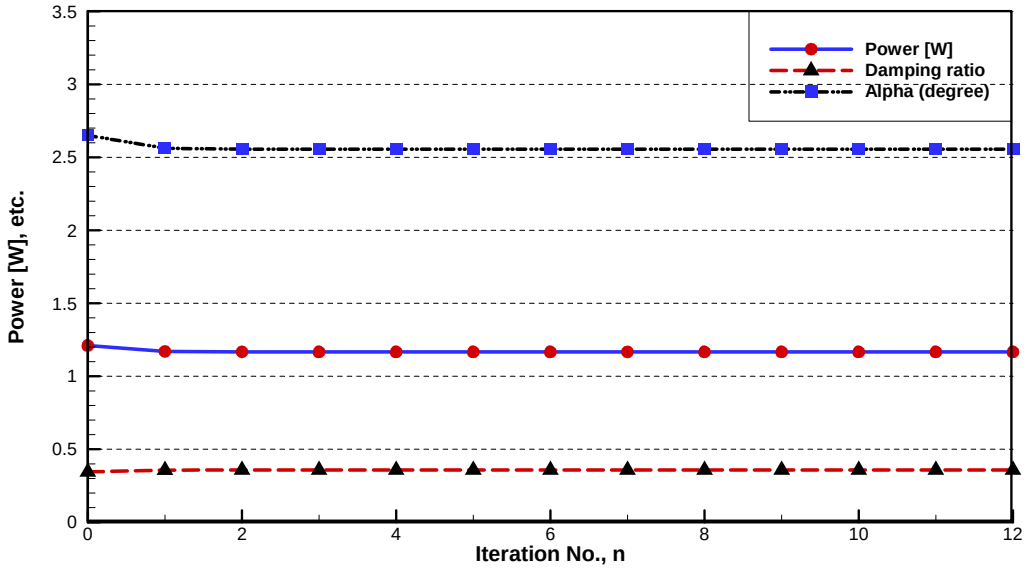

Figure 15 Convergence at Δp = 0.2 bar for one regular wave case (H=1.0 m, T=6.0 sec) using WEC-2 (surge only)

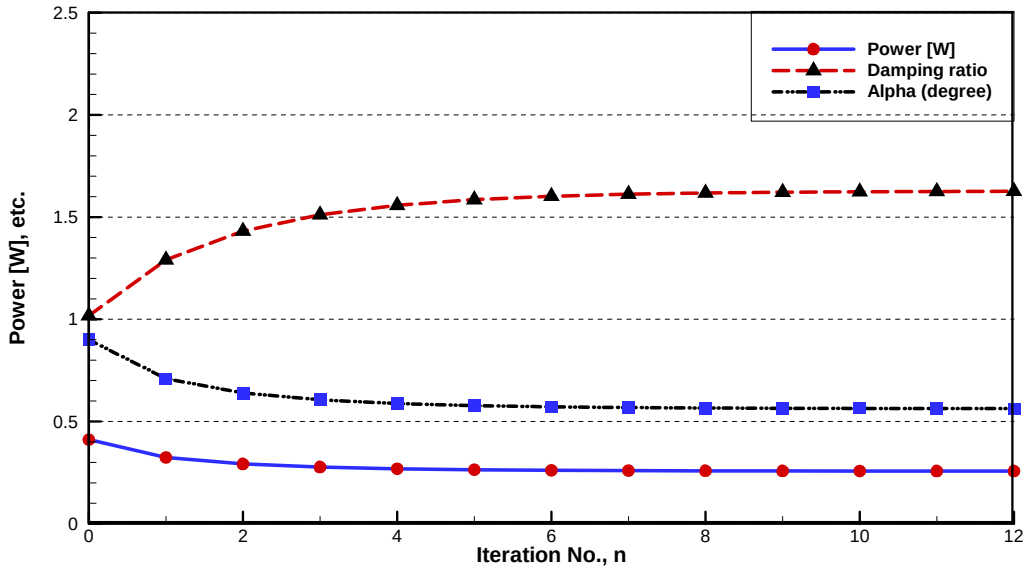

Figure 16 Convergence at Δp = 0.2 bar for one regular wave case (H=1.0 m, T=6.0 sec) using WEC-2 (pitch only)

Figs. 17-20 show the converged electrical power outputs for the two WEC cases at various pressure differences between the HP accumulator and the LP tank. Amplitudes obtained using FFT is used for the computing results Fig. 17 and Fig. 19. Amplitudes taken as a half of peak to trough value are used for the computing results Fig. 18 and Fig. 20. The optimum power rates and the pressure differences are summarized in Table 7. It should be noted that the estimated power outputs based on the amplitude obtained using FFT are conservative because the accelerations induced by the second harmonic are not included.

The table shows that optimum generations by two WEC devices rate 1.42 W - 2.20 W and 2.28 W - 3.45 W in the regular wave (H=1.0 m, T=6.0 sec). The results also

indicate that each configuration of WEC devices produces its optimum power output at a unique pressure difference. The power outputs decrease dramatically when the pressure difference is beyond of the 'optimal' pressure difference. When the pressure difference is above of 0.76 for FFT use (or 0.93 bar for a half of peak to trough value use), the WEC devices simply do not produce electrical power because the estimated equivalent damping coefficient is too large. In other words, the large resistance provided by the piston induced by the large pressure difference stops the wheel to oscillate.

The plots and table also show that contributions from pitch motions are much smaller than from surge motions. Furthermore, beyond certain pressure differences, pitch does not produce any energy, but surge does. Thus, the optimum powers for the most occurring wave condition are contributed from surge motions except for Fig. 18. However, the contribution of surge and pitch depends on the WEC dimension, wave frequency, and motion results which are elements of $M(t)$. Thus, the statement for which motion critically contributes to electric power generation cannot be generalized for all of SEAREV type devices.

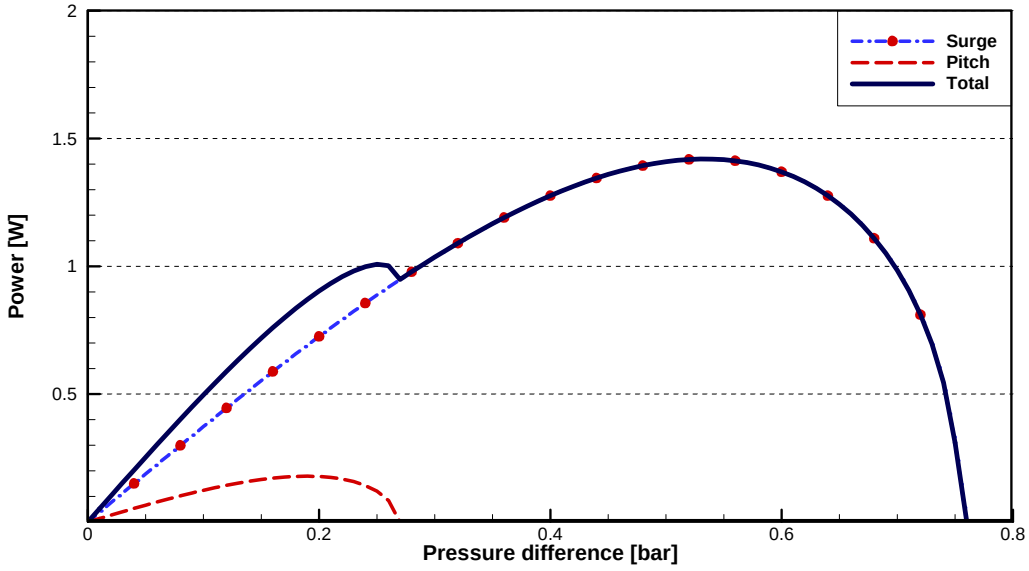

Figure 17 Power output for one regular wave case (H=1.0 m, T=6.0 sec) using WEC-1 and FFT data

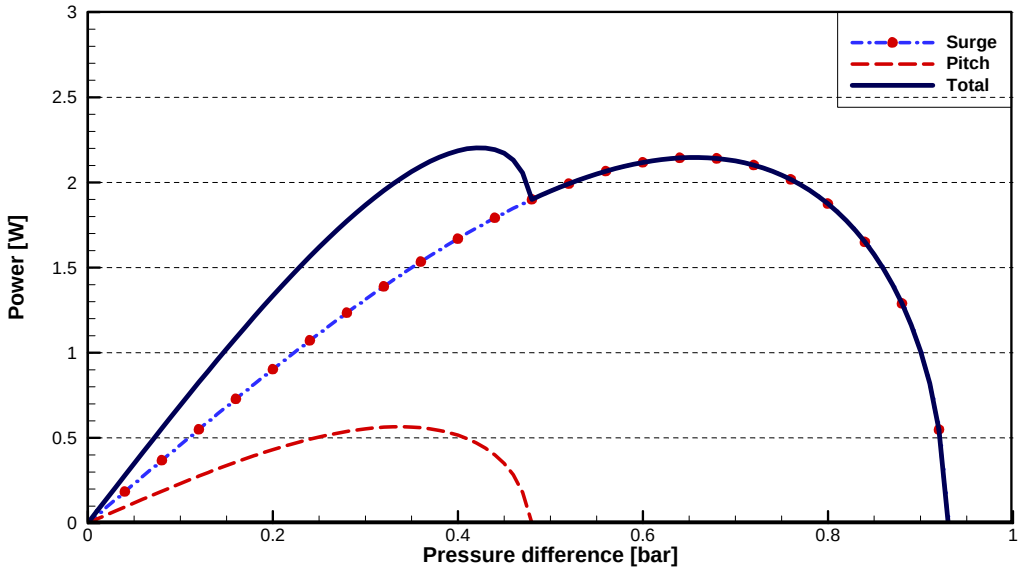

Figure 18 Power output for one regular wave case (H=1.0 m, T=6.0 sec) using WEC-1 and a half of peak to trough value

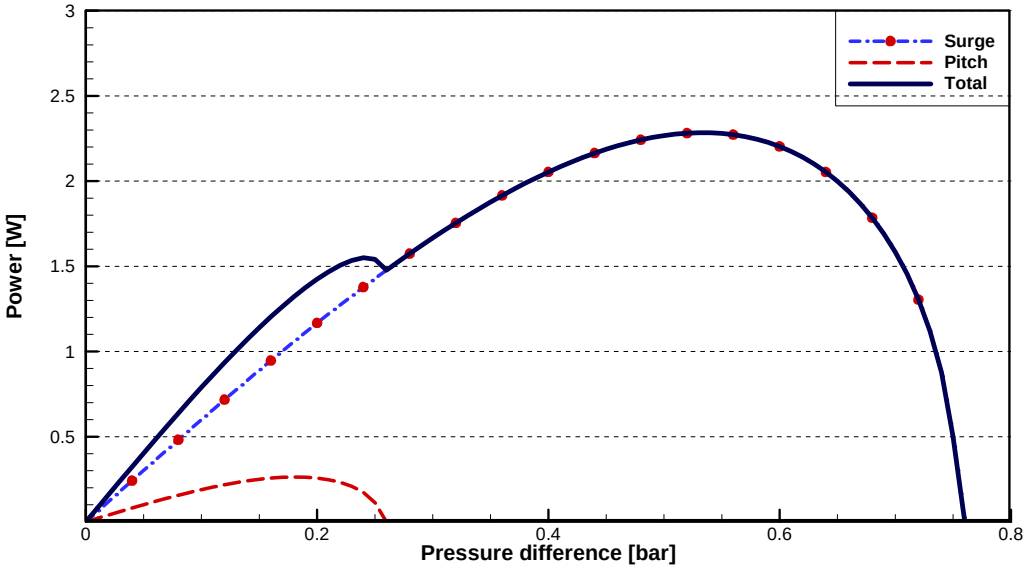

Figure 19 Power output for one regular wave case (H=1.0 m, T=6.0 sec) using WEC-2 and FFT data

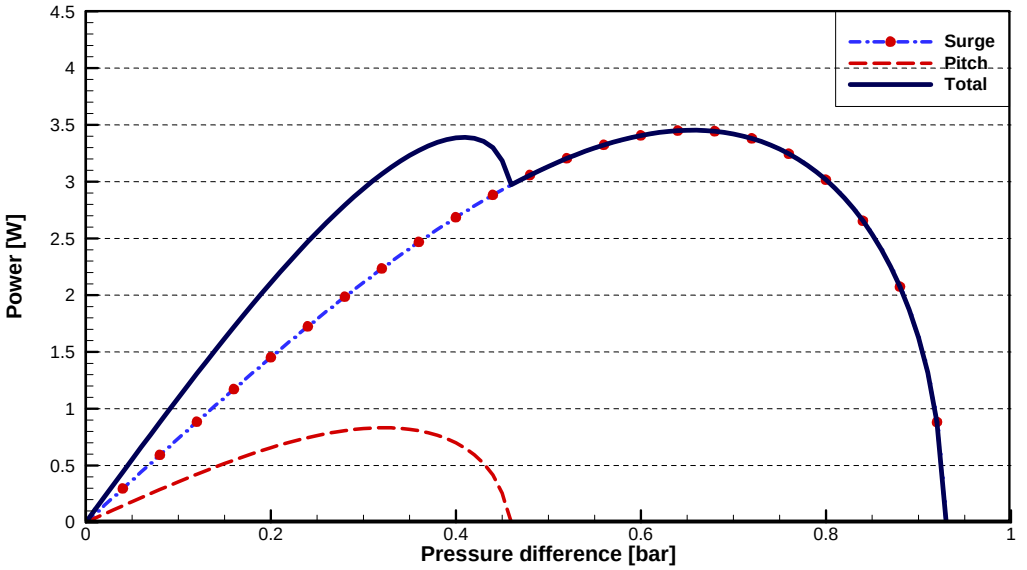

Figure 20 Power output for one regular wave case (H=1.0 m, T=6.0 sec) using WEC-2 and a half of peak to trough value

Table 7 Summary of power output for one regular wave case (H=1.0 m, T=6.0 sec)

Motion/Item \ Use of data		A half of peak to trough value		FFT	
		WEC-1	WEC-2	WEC-1	WEC-2
Surge	Optimum power	2.15 W	3.45 W	1.42 W	2.28 W
	At pressure difference	0.66 bar	0.66 bar	0.53 bar	0.53 bar
Pitch	Optimum power	0.57 W	0.83 W	0.18 W	0.26 W
	At pressure difference	0.34 bar	0.32 bar	0.19 bar	0.18 bar
Total	Optimum power	2.20 W	3.45 W	1.42 W	2.28 W
	At pressure difference	0.42 bar	0.66 bar	0.53 bar	0.53 bar

4.3.2 Weighted Average Power Output for the Ten Regular Wave Cases

The yearly average power output is estimated based on the summation of the power output of the ten wave conditions multiplied by the related occurrence probability in each year. In computing the power output of each wave condition, the pressure difference is kept as a constant. Figs. 21-24 show the estimated average power output for the two WEC cases at various pressure differences. The surge and pitch amplitudes obtained using FFT is used for Fig. 21 and Fig. 23, while the amplitudes obtained as a half of peak to trough value are used for Fig. 22 and Fig. 24. The optimum power rates and the pressure differences are summarized in Table 8. Table 8 shows that optimum power generations by two WEC devices rate 1.69 W - 2.88 W and 2.76 W – 4.55 W.

When the pressure difference is kept at 0.59 – 0.63 bar, the power outputs from both WEC-1 and WEC-2 roughly reach the optimum values. Tables 9-12 show the results at pressure difference at 0.60 bar. Comparing the amplitudes of the floating body listed in Table 6 to power outputs in Tables 9-12, it is shown that a large motion results in large power output. The pitch amplitudes based on the FFT data do not contribute to the optimum power generation at all for both WEC devices. Also, at some wave conditions there are no power output generated by either pitch or surge. In particular, there is no contribution from the wave conditions H=0.5m, T=6.0 sec and H=1.0m, T=7.0 sec when using amplitudes based on the FFT data because M_{pitch} *(t) and* M_{surge} *(t),* the moment excited by them, are too small to overcome the resistance for pushing the piston. This is mainly caused by two factors: one is small amplitudes of surge and pitch induced by small wave height and the other is small wave frequency, both of which reduce the related accelerations and hence M_{pitch} *(t) and* M_{surge} *(t)*. Additionally, in our case, the wave frequency is far apart from the natural frequency of the pendulum system.

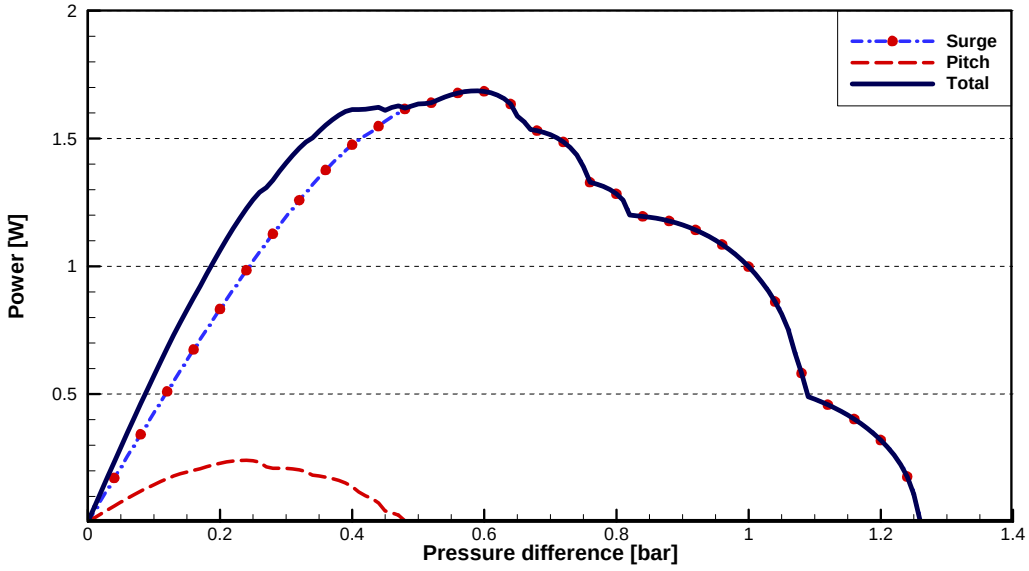

Figure 21 Weighted average power output for the ten regular wave cases using WEC-1 and FFT data

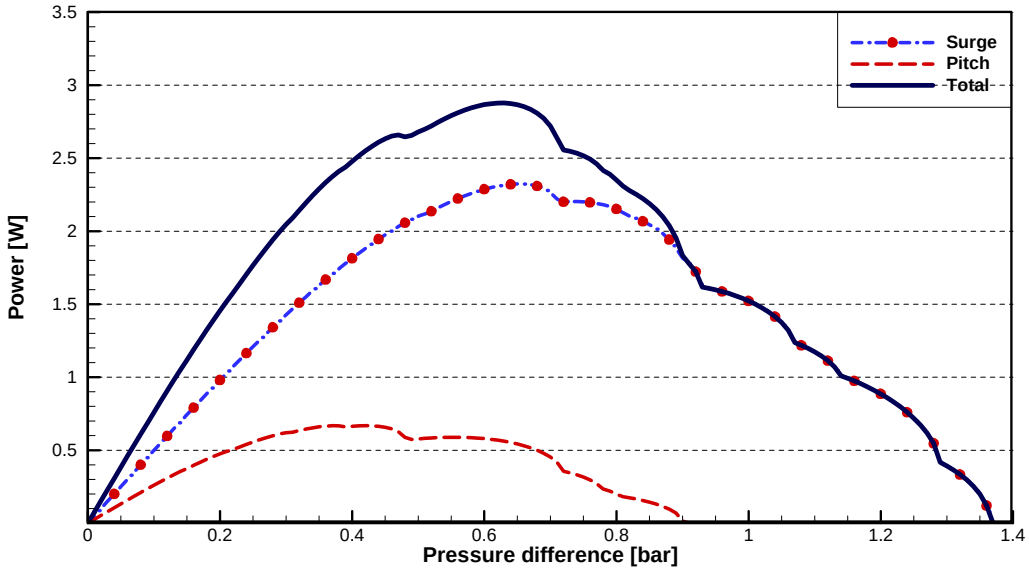

Figure 22 Weighted average power output for the ten regular wave cases using WEC-1 and a half of peak to trough value

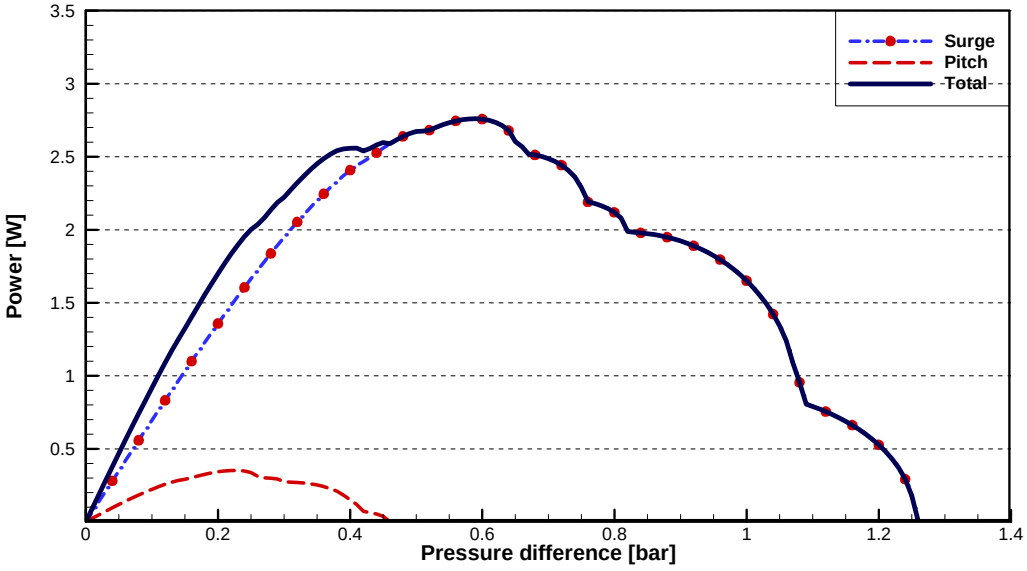

Figure 23 Weighted average power output for the ten regular wave cases using WEC-2 and FFT data

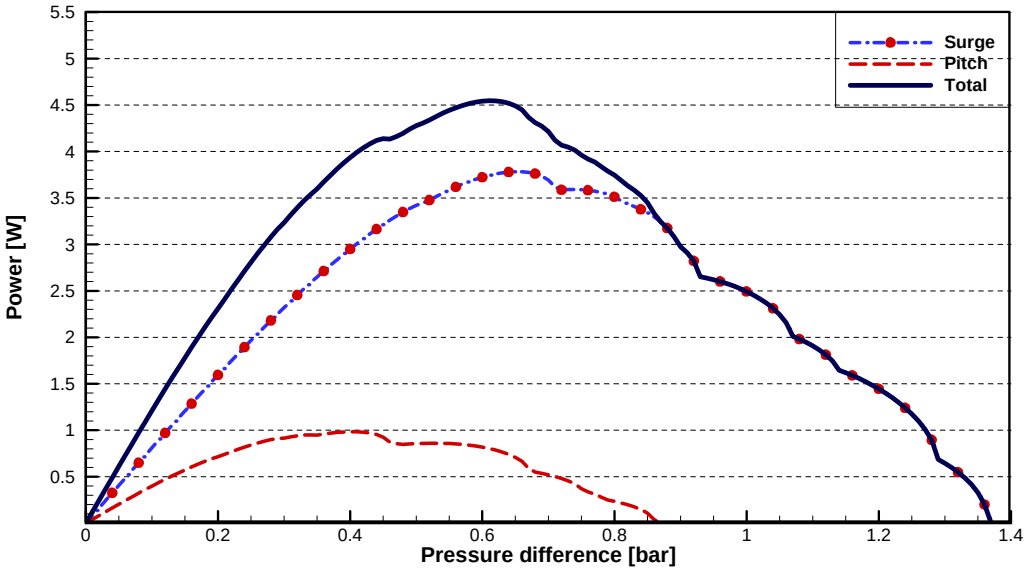

Figure 24 Weighted average power output for the ten regular wave cases using WEC-2 and a half of peak to trough value

Table 8 Summary of weighted average power output for the ten regular wave cases

Motion/Item \ Use of data		A half of peak to trough value		FFT	
		WEC-1	WEC-2	WEC-1	WEC-2
Surge	Optimum power	2.32 W	3.78 W	1.69 W	2.76 W
	At pressure difference	0.65 bar	0.65 bar	0.59 bar	0.59 bar
Pitch	Optimum power	0.67 W	0.98 W	0.24 W	0.35 W
	At pressure difference	0.42 bar	0.40 bar	0.24 bar	0.23 bar
Total	Optimum power	2.88 W	4.55 W	1.69 W	2.76 W
	At pressure difference	0.63 bar	0.61 bar	0.59 bar	0.59 bar

Table 9 Power by WEC-1 and its variable at Δp =0.6 bar (FFT data)

T	H	P [W]		ζ [-]		$\alpha_{i=0}$ [°]		$\alpha_{i=N}$ [°]		$\lambda_{i=N}$ [cm]	
[s]	[m]	Surge	Pitch	Surge	Pitch	Surge	Pitch	Surge	Pitch	Surge	Pitch
4	0.5	4.43	-	0.68	-	4.00	-	3.32	-	64.96	-
5	0.5	1.07	-	2.84	-	2.32	-	1.00	-	65.00	-
	1.0	4.11	-	0.74	-	4.37	-	3.84	-	64.95	-
6	0.5	-	-	-	-	-	-	-	-	-	-
	1.0	1.37	-	2.22	-	2.53	-	1.54	-	64.99	-
	1.5	2.72	-	1.12	-	3.66	-	3.05	-	64.97	-
7	1.0	-	-	-	-	-	-	-	-	-	-
	1.5	0.63	-	4.84	-	2.14	-	0.82	-	65.00	-
	2.0	1.40	-	2.17	-	2.69	-	1.84	-	64.99	-
8	2.0	1.21	-	2.51	-	2.66	-	1.81	-	64.99	-

Table 10 Power by WEC-1 and its variable at Δp =0.6 bar (a half of peak to trough value)

T	H	P [W]		ζ [-]		$\alpha_{i=0}$ [°]		$\alpha_{i=N}$ [°]		$\lambda_{i=N}$ [cm]	
[s]	[m]	Surge	Pitch	Surge	Pitch	Surge	Pitch	Surge	Pitch	Surge	Pitch
4	0.5	4.40	-	0.69	-	3.99	-	3.30	-	64.96	-
5	0.5	1.43	-	2.12	-	2.48	-	1.34	-	64.99	-
	1.0	4.57	1.47	0.67	2.07	4.76	2.50	4.27	1.37	64.94	64.99
6	0.5	-	-	-	-	-	-	-	-	-	-
	1.0	2.12	-	1.43	-	3.12	-	2.38	-	64.98	-
	1.5	3.41	2.01	0.89	1.51	4.33	3.03	3.83	2.26	64.95	64.98
7	1.0	0.93	-	3.28	-	2.32	-	1.21	-	65.00	-
	1.5	1.66	-	1.82	-	2.94	-	2.18	-	64.98	-
	2.0	2.42	1.23	1.25	2.46	3.74	2.55	3.17	1.62	64.97	64.99
8	2.0	1.17	1.15	2.56	2.64	2.63	2.60	1.77	1.72	64.99	64.99

Table 11 Power by WEC-2 and its variable at Δp =0.6 bar (FFT data)

T	H	P [W]		ζ [-]		$\alpha_{i=0}$ [°]		$\alpha_{i=N}$ [°]		$\lambda_{i=N}$ [cm]	
[s]	[m]	Surge	Pitch	Surge	Pitch	Surge	Pitch	Surge	Pitch	Surge	Pitch
4	0.5	7.65	-	0.49	-	4.50	-	3.73	-	99.93	-
5	0.5	1.76	-	2.14	-	2.48	-	1.07	-	99.99	-
	1.0	6.76	-	0.56	-	4.68	-	4.11	-	99.91	-
6	0.5	-	-	-	-	-	-	-	-	-	-
	1.0	2.20	-	1.71	-	2.65	-	1.68	-	99.99	-
	1.5	4.37	-	0.86	-	3.82	-	3.19	-	99.95	-
7	1.0	-	-	-	-	-	-	-	-	-	-
	1.5	1.00	-	3.78	-	2.21	-	0.85	-	100.00	-
	2.0	2.23	-	1.69	-	2.78	-	1.90	-	99.98	-
8	2.0	1.99	-	1.97	-	2.72	-	1.86	-	99.98	-

Table 12 Power by WEC-2 and its variable at Δp =0.6 bar (a half of peak to trough value)

T	H	P [W]		ζ [-]		$\alpha_{i=0}$ [°]		$\alpha_{i=N}$ [°]		$\lambda_{i=N}$ [cm]	
[s]	[m]	Surge	Pitch	Surge	Pitch	Surge	Pitch	Surge	Pitch	Surge	Pitch
4	0.5	7.61	-	0.49	-	4.48	-	3.70	-	99.93	-
5	0.5	2.36	-	1.60	-	2.65	-	1.43	-	99.99	-
	1.0	7.51	1.84	0.50	2.04	5.09	2.50	4.57	1.12	99.89	99.99
6	0.5	-	-	-	-	-	-	-	-	-	-
	1.0	3.41	-	1.10	-	3.26	-	2.46	-	99.97	-
	1.5	5.49	2.97	0.69	1.27	4.53	3.03	4.01	2.17	99.92	99.98
7	1.0	1.47	-	2.56	-	2.39	-	1.25	-	99.99	-
	1.5	2.64	-	1.42	-	3.03	-	2.25	-	99.97	-
	2.0	3.85	1.80	0.98	2.09	3.86	2.55	3.28	1.53	99.95	99.99
8	2.0	1.87	1.72	2.02	2.19	2.70	2.60	1.82	1.67	99.98	99.99

4.3.3 Power Output for Various Positions of WEC Device

This section explores the effect of the parameter *d* on the power output, when the *d* is distance from the center of gravity of the buoy, G, to the pivot point of the wheel A. This is a parameter to decide the magnitude of M_{pitch} *(t)*. Figs. 25-28 show the variance of power generation with the change of *d,* taking WEC-2 (FFT data) as an example. Because the contribution from pitch is much smaller than surge by the given dimensions of WECs, only small variances by position changes are shown. Total power outputs

beyond certain pressure levels do not have any variance with the change of *d* because at this pressure range only surge that does not have correlation with *d* contributes to the power generation.

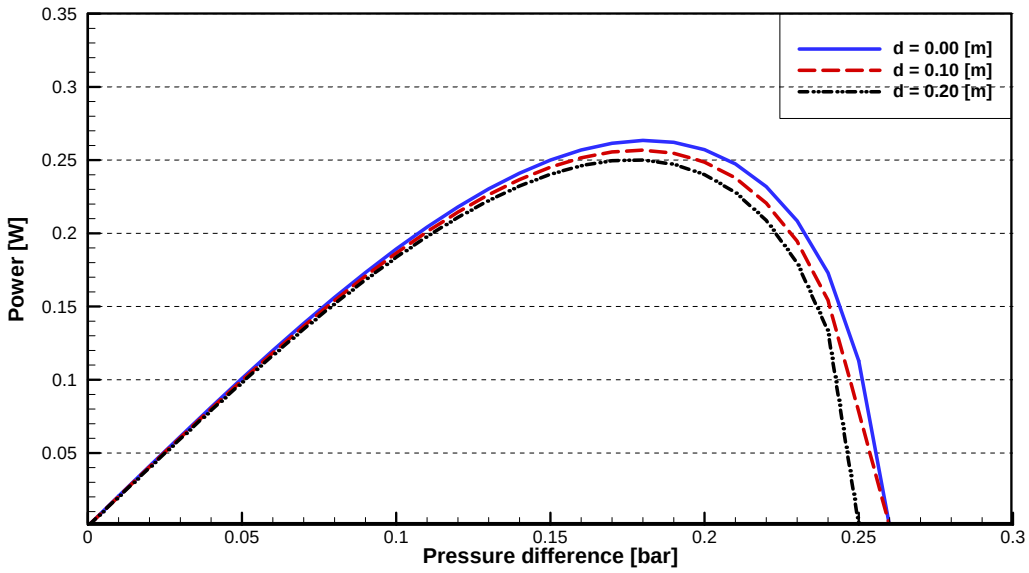

Figure 25 Power outputs for one regular wave case (H=1.0 m, T=6.0 sec) depending on WEC positions (pitch only)

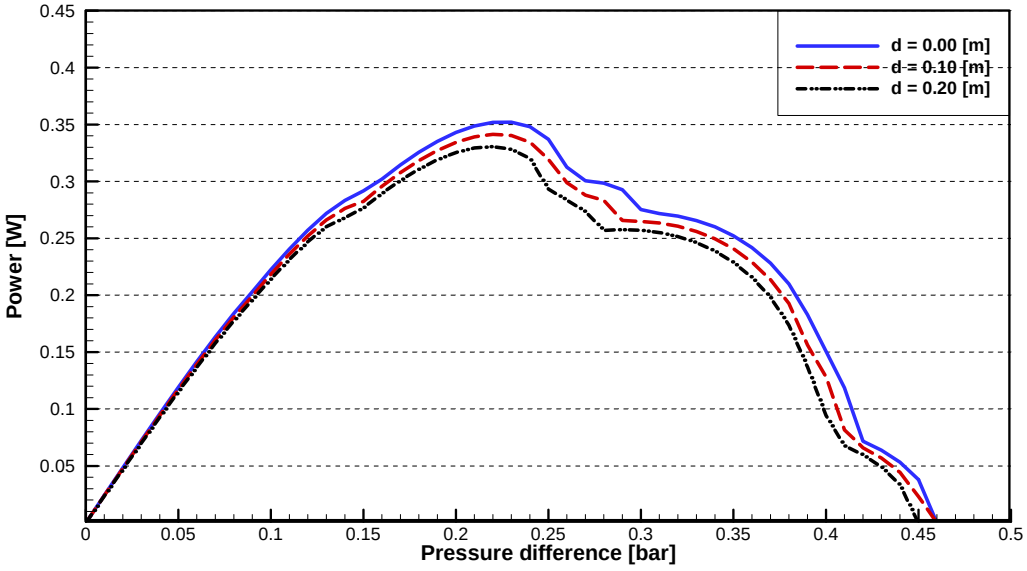

Figure 26 Power outputs for the ten regular wave cases depending on WEC positions (pitch only)

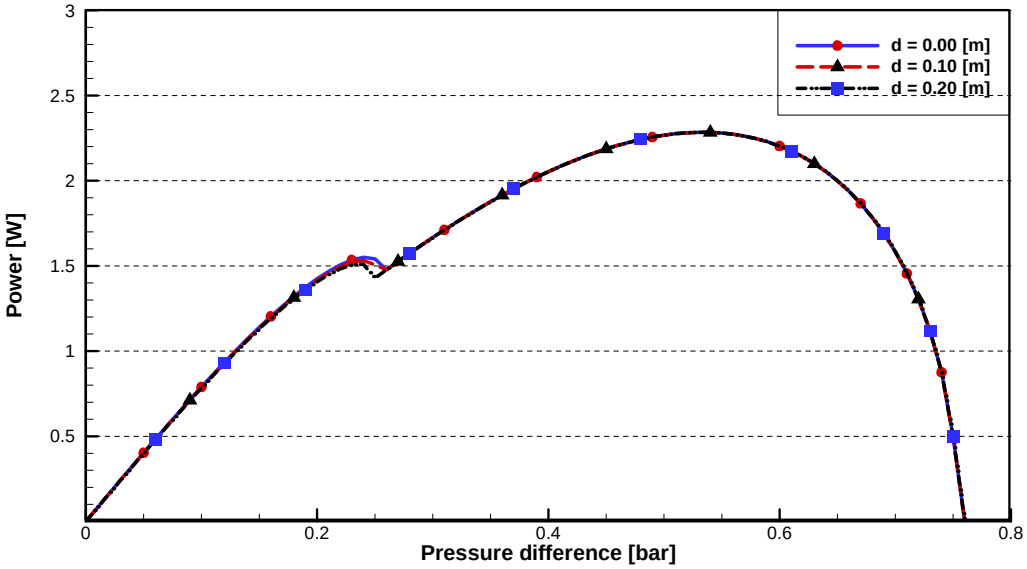

Figure 27 Power outputs for one regular wave case (H=1.0 m, T=6.0 sec) depending on WEC positions (total)

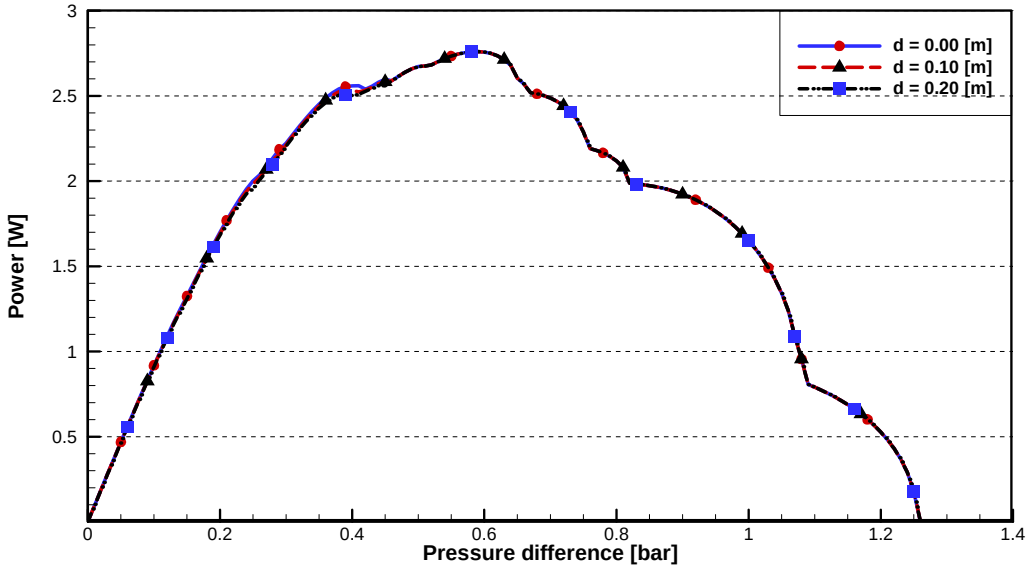

Figure 28 Power outputs for the ten regular wave cases depending on WEC positions (total)

4.3.4 Power Output by Two Hydraulic Cylinders

The space after arranging the inner pendulum in the center of the buoy allows installation of an additional hydraulic cylinder on the opposite side as shown in Fig. 29.

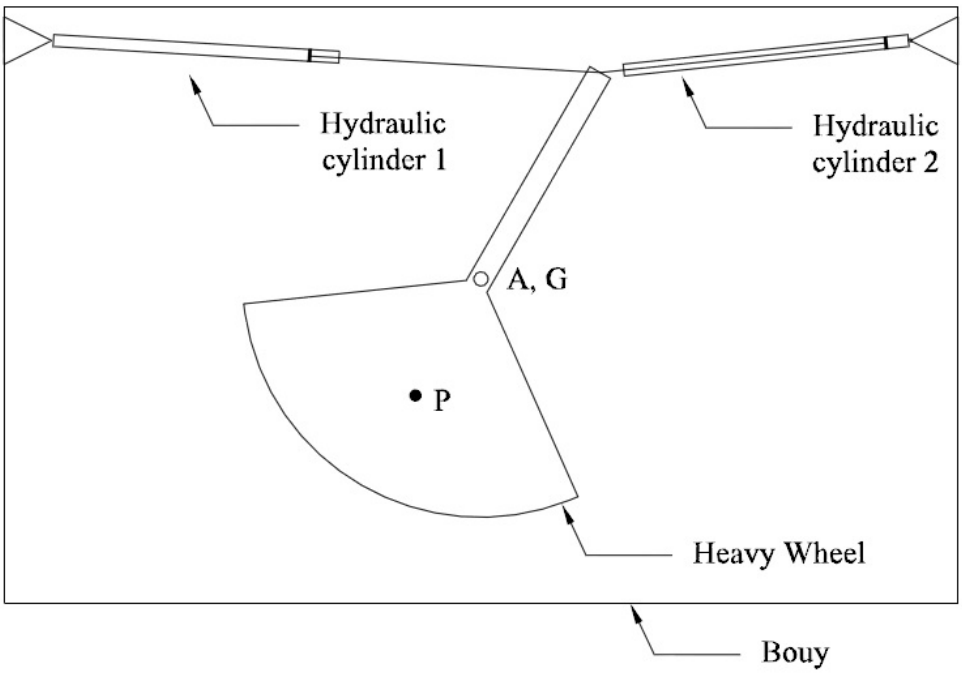

Figure 29 Arrangement of two hydraulic cylinders

The power outputs by two hydraulic cylinders are simulated based on the fact that both power estimation and damping are twice the amount of them in the case of one hydraulic cylinder. The simulation results below are for WEC-2 and FFT data. As shown in Fig. 30, the additional hydraulic cylinder set may be more effective than single cylinder set in the relatively low pressure difference range, but the single cylinder set is more effective in the relatively high pressure difference range. Thus, if the pressure difference is decided, the number of hydraulic cylinder set can be decided for work efficacy.

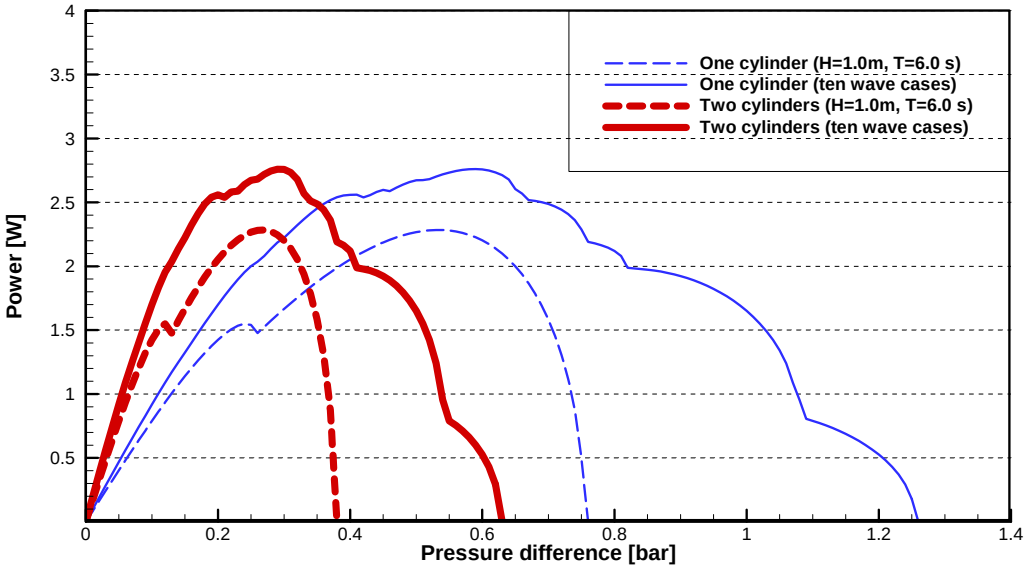

Figure 30 Power outputs for one/two hydraulic cylinders Power Take-Off system

CHAPTER V

CONCLUSIONS AND FUTURE WORK

5.1 Conclusions

This study explores the idea of utilizing a Wave Energy Conversion (WEC) device to provide electric energy for oceanographic buoys as a permanent or semi-permanent power source. A WEC device of SEAREV type that can be modeled as a pendulum set was selected because of utilizing its simplicity and reliability, and minimizing the potential for vandalism and stealing of a current power source. The numerical simulations for estimating the power outputs of the WEC devices with sizes which can be housed by typical oceanographic buoys are performed and confirm their feasibility.

The method of estimating power outputs mainly consists of three steps. First, the motions of the floating buoy moored by its mooring system under the impact of various regular waves are calculated using an in-house code, COUPLE. Secondly, the oscillation of the wheel is estimated based on the surge and pitch motions of the buoy. In this research study, the oscillation of the pendulum set is explained by two approaches. One is a Lagrange's approach. The other is a Newtonian approach, which was already performed by the earlier study on SEAREV. Thirdly, the oscillation of the wheel is re-estimated by allowing for the damping coefficient resulting from the energy consumed for driving the piston through an iterative scheme. After the convergence of the damping coefficient is reached, the electrical power outputs are obtained. Using the iterative

scheme, the parametric studies with pressure difference are performed in order to find the optimum power output and its pressure condition of the hydraulic Power Take-Off (PTO) system.

Comparing the results from this study to power demands for typical oceanographic buoys, it can be concluded that the proposed WEC device is feasible. Further, this study examines the contributions of motions, mainly surge and pitch, to the power generation. For the cases of typical oceanographic buoys and the pendulum wheel proposed in this study, surge acceleration seems to contribute most to the excitation of the pendulum oscillation hence to the generation of electrical power.

Findings made in this study and performing coupled dynamic analysis for the use of a WEC device of SEAREV type may have valuable applications to the design of this device used as a renewable energy source in a wide range of shapes and different sizes of oceanographic buoys with various mooring configurations in the future.

5.2 Future Work

The estimated power can be increased by optimizing a few parameters of the WEC, such as a pendulum length, mass and its centroidal moment of inertia of the inner pendulum wheel, the center of gravity of the buoy, mooring arrangement. Evaluation of these parameters can produce the optimized power output within the dimensions of the hull described in this study.

Another improvement can be achieved by changing the wheel type, which is currently proposed and arranged in order to mainly utilize horizontal accelerations by

surge and pitch motions. The current pendulum type achieves its maximum efficiency under the condition that a wave direction is on the plane of two-dimensional motions. In order to overcome this drawback, attaching an additional pendulum wheel, which is perpendicular to the current wheel or a wheel rotating on a horizontal plane, helps the PTO to additionally obtain energy from sway, roll, or yaw motion.

Furthermore, since the 6-DOF motions of a moored buoy under the impact of irregular ocean waves can be predicted using COUPLE, the estimated power output of the related WEC devices can be extended for the cases of irregular waves.

REFERENCES

Ahmad, S. (1996). Stochastic TLP response under long crested random sea. *Computers & Structures*, *61*(6), pp 975-993.

Babarit, A. (2005). *Optimisation hydrodynamique et contrôle optimal d'un récupérateur d 'énergie des vagues* (Doctoral dissertation). Ecole Centrale de Nantes, Nantes, France. pp 1-51.

Babarit, A., Clement, A. H., Ruer J., & Tartivel, C. (2006). SEAREV: A fully integrated wave energy converter. Proceedings of *Offshore Wind and Other Marine Renewable Energies in Mediterranean and European Seas Seminar*, Rome, Italy.

Babarit, A., Mouslim, H., Guglielmi, M., & Clement, A. H. (2008). Simulation of the SEAREV wave energy converter with a by-pass control of its hydraulic power take off. Proceedings of *the 10th World Renewable Energy Congress*, Glasgow, UK, pp 1004-1009.

Baruh, H. (1999). *Analytic dynamics* (International ed.). New York: McGraw-Hill. pp 97-107, 215-272, 367-378.

Berteaux, H. O. (1991). *Coastal and oceanic buoy engineering*. Taunton, MA: Author. pp 11-20.

Chen, X. (2002). *Studies on dynamics interaction between deep-water floating structures and their mooring/tendon systems* (Doctoral dissertation). Texas A&M University, College Station, TX. pp 1-60.

Falcao, A. F. O. (2007). Modelling and control of oscillating-body wave energy converters with hydraulic power take-off and gas accumulator. *Ocean Engineering*, *34*(14), pp 2021-2032.

Faltinsen, O. M. (1990). *Sea loads on ships and offshore structures*. Cambridge UK: Cambridge University Press. pp 61, 223-225.

Garrett, D. L. (1982). Dynamic analysis of slender rods. *Journal of Energy Resources Technology*, *104*(4), pp 302-306.

Henderson, A., & Patel, M. (1998). Rigid-body motion of a floating offshore windfarm. *International Journal of Ambient Energy*, *19*(3), pp 127-134.

Jain, A. K. (1997). Nonlinear coupled response of offshore tension leg platforms to regular wave forces. *Ocean Engineering*, *24*(7), pp 577-592.

Jia, D. (2012). *An efficient numerical scheme for simulating unidirectional irregular waves based on a hybrid wave model* (Master's thesis). Texas A&M University, College Station, TX. pp 1-50.

Josset, C., Babarit, A., & Clement, A. H. (2007). A wave-to-wire model of the SEAREV wave energy converter. Proceedings of *the Institution of Mechanical Engineers, Part M: Journal of Engineering for the Maritime Environment*, *221*, pp 81-93.

Lee, C. H. (1995). *WAMIT theory manual: Report No. 95-2*. Massachusetts Institute of Technology, Cambridge, MA. pp 28-31.

Ma, W., & Webster, W. C. (1994). *An analytical approach to cable dynamics: Theory and user manual*. Sea Grant Poject R/OE-26.

Meinig, C. (2013). Private communication.

NDBC. (2008, February 4). Moored buoy program. Retrieved from http://www.ndbc.noaa.gov/mooredbuoy.shtml

NDBC. (2013). Station ID search. Retrieved December 1, 2013, from http://www.ndbc.noaa.gov/

Nikravesh, P. E. (1988). *Computer-aided analysis of mechanical systems*. Englewood Cliffs, NJ: Prentice-Hall. pp 347-352.

Paulling, J. R., & Webster, W. C. (1986). A consistent large-amplitude analysis of the coupled response of a TLP and tendon system. Proceedings of *Offshore Mechanics and Arctic Engineering*, Tokyo, Japan, *3*, pp 126-133.

Pettigrew, B., & Pigeon, R. (2013). Private communication.

Ruellan, M., BenAhmed, H., Multon B., Josset, C., Babarit, A., & Clement, A. H. (2007). Design methodology for a SEAREV wave energy converter. Proceedings of *the IEEE International Electric Mechines and Device Conference*, Antalya, Turkey, pp 1384-1389.

Ruellan, M., BenAhmed, H., Multon B., Josset, C., Babarit, A., & Clement, A. H. (2010). Design methodology for a SEAREV wave energy converter. *IEEE Transactions on Energy Conversion*, *25*(3), pp 760-767.

Spell, C. A., Zhang, J., & Randall, R. E. (1996). Hybrid Wave Model for unidirectional irregular waves-Part II. Comparison with laboratory measurements. *Applied Ocean Research*, *18*, pp 93-110.

Teng, C-C., Cucullu, S., McArthur, S., Kohler, C., Burnett, B., & Bernard, L. (2009). Buoy vandalism experienced by NOAA National Data Buoy Center. Proceedings

of *Oceans' 09. MTS/IEEE-Marine technology for our future: Global and local challenges*, Biloxi, MS, OCEANS, pp 1-8.

Timpe, G., & Teng, C-C. (1992). Developing design criteria for use in data buoy design. Proceedings of *Oceans' 92. Mastering the oceans through technology*, Newport, RI, *2*, pp 764-769.

Thomson, W. T. (1972). *Theory of vibration with applications*. Englewood Cliffs, NJ: Prentice-Hall. pp 300-302

Zhang, J., Chen, L., Ye, M., & Randall, R. E. (1996). Hybrid Wave Model for unidirectional irregular waves-Part I. Theory and numerical scheme. *Applied Ocean Research*, *18*, pp 77-92.

Zhang, J. (2014). Private communication.

APPENDIX A

EULER ANGLES

Euler angles are used to refer to three angles for transforming into one coordinate set from another (Baruh, 1999). The idea of transformations comes from the fact that at most three successive rotations, in which no two adjacent rotation indices are the same, can transform an orthogonal right-handed three dimensional Cartesian coordinate system into any other orthogonal right-handed three dimensional Cartesian coordinate systems. In generating the three sets of rotations, the possible options are limited to twelve choices, 1-2-1, 1-2-3, 1-3-1, 1-3-2, 2-1-2, 2-1-3, 2-3-1, 2-3-2, 3-1-2, 3-1-3, 3-2-1, and 3-2-3, and are called Euler angle sequences. When used with a space-fixed coordinate system, the angles describe the orientation of a rigid body with respect to the spaced fixed coordinates. Previous studies (Chen, 2002) and software COUPLE have used the roll-pitch-yaw, or 1-2-3, sequence for the Euler angles $\boldsymbol{\alpha} = (\alpha_1, \alpha_2, \alpha_3)^T$.

Fig. 31 shows how to build a rotation matrix taking an example of only one element of the Euler angles. Consider an initial frame $a_1 a_2 a_3$, and rotate it by an angle of α_1 about the a_1 axis. Denoting the resulting frame by $a_1' a_2' a_3'$, the following relationship is made (Baruh, 1999):

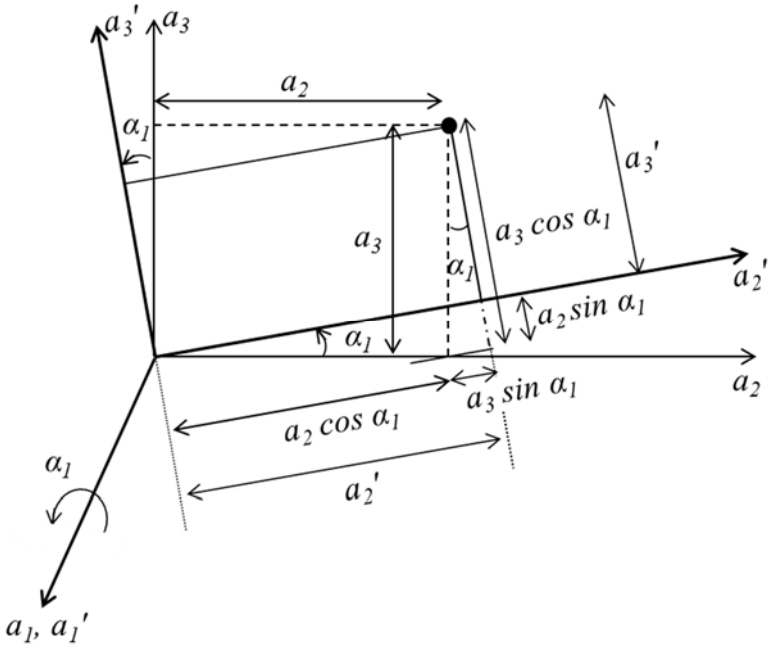

Figure 31 A rotation and coordinates

$$\begin{cases} a_1' = a_1 \\ a_2' = a_2 \cos\alpha_1 + a_3 \sin\alpha_1 \\ a_3' = -a_2 \sin\alpha_1 + a_3 \cos\alpha_1 \end{cases} \tag{22}$$

This can be expressed in the matrix form of

$$\{a'\} = \begin{bmatrix} 1 & 0 & 0 \\ 0 & \cos\alpha_1 & \sin\alpha_1 \\ 0 & -\sin\alpha_1 & \cos\alpha_1 \end{bmatrix} \{a\} \tag{23}$$

where, $\{a\} = [a_1, a_2, a_3]^{\mathrm{T}}$ and $\{a'\} = [a_1', a_2', a_3']^{\mathrm{T}}$.

In order to complete the transformation of roll-pitch-yaw sequence, taking the same rotation procedure to the transformed coordinate about a_2' yields $a_1'' a_2'' a_3''$ axes.

Then, another successive rotation of $a_1''a_2''a_3''$ coordinate about a_3'' yields $b_1b_2b_3$ axes.

The transformation can be expressed in the matrix form of Eq. 24 and Eq. 25.

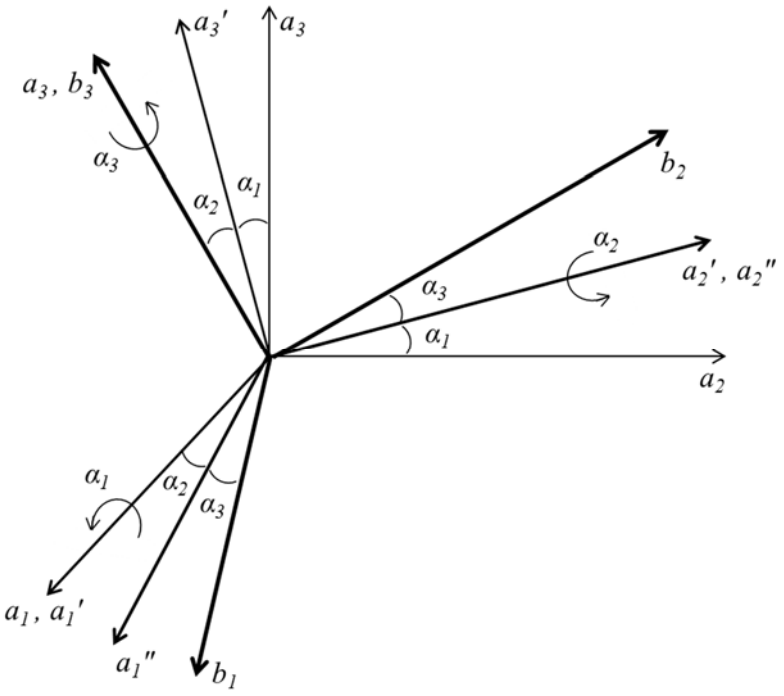

Figure 32 Rotations and Euler angles (Nikravesh, 1988)

$$\{a''\} = \begin{bmatrix} \cos\alpha_2 & 0 & -\sin\alpha_2 \\ 0 & 1 & 0 \\ \sin\alpha_2 & 0 & \cos\alpha_2 \end{bmatrix} \{a'\} \tag{24}$$

$$\{b\} = \begin{bmatrix} \cos\alpha_3 & \sin\alpha_3 & 0 \\ -\sin\alpha_3 & \cos\alpha_3 & 0 \\ 0 & 0 & 1 \end{bmatrix} \{a''\} \tag{25}$$

Thus, the following relationship is made.

$$\{b\} = \mathbf{T}\{a\} \tag{26}$$

where,

$$\mathbf{T} = \begin{bmatrix} \cos\alpha_3 \cos\alpha_2 & \sin\alpha_3 \cos\alpha_1 + \cos\alpha_3 \sin\alpha_2 \sin\alpha_1 & \sin\alpha_3 \sin\alpha_1 - \cos\alpha_3 \sin\alpha_2 \cos\alpha_1 \\ -\sin\alpha_3 \cos\alpha_2 & \cos\alpha_3 \cos\alpha_1 - \sin\alpha_3 \sin\alpha_2 \sin\alpha_1 & \cos\alpha_3 \sin\alpha_1 + \sin\alpha_3 \sin\alpha_2 \cos\alpha_1 \\ \sin\alpha_2 & -\cos\alpha_2 \sin\alpha_1 & \cos\alpha_2 \cos\alpha_1 \end{bmatrix} \tag{27}$$

T is also a transfer matrix between the space-fixed coordinates $\hat{\mathbf{x}}=(\hat{x},\hat{y},\hat{z})^{\mathrm{T}}$ and the body-fixed coordinate $\mathbf{x}=(x,y,z)^{\mathrm{T}}$ in COUPLE as below. The matrix is orthogonal with the property that $\mathbf{T}^{\mathrm{t}} = \mathbf{T}^{-1}$.

$$\hat{\mathbf{x}} = \boldsymbol{\xi} + \mathbf{T}^{\mathrm{t}}\mathbf{x} \tag{28}$$

where, $\boldsymbol{\xi}$ is a translational displacement between body-fixed coordinates and space-fixed coordinates, and the superscript **t** indicates the transpose of a matrix.

The derivatives of the Euler angles $(\dot{\alpha}_1, \dot{\alpha}_2, \dot{\alpha}_3)^{\mathrm{T}}$ can be separated along the directions of the coordinate, $b_1 b_2 b_3$ axes (Nikravesh, 1988).

$$\begin{cases} \dot{\alpha}_{1\,(b_1)} = \dot{\alpha}_1 \cos\alpha_3 \cdot \cos\alpha_2 \\ \dot{\alpha}_{1\,(b_2)} = \dot{\alpha}_1 \cos\alpha_2 \cdot (-\sin\alpha_3) \\ \dot{\alpha}_{1\,(b_3)} = \dot{\alpha}_1 \sin\alpha_2 \end{cases} \tag{29}$$

$$\begin{cases} \dot{\alpha}_{2\,(b_1)} = \dot{\alpha}_2 \sin\alpha_3 \\ \dot{\alpha}_{2\,(b_2)} = \dot{\alpha}_2 \cos\alpha_3 \\ \dot{\alpha}_{2\,(b_3)} = 0 \end{cases} \tag{30}$$

$$\begin{cases} \dot{\alpha}_{3\,(b_1)} = 0 \\ \dot{\alpha}_{3\,(b_2)} = 0 \\ \dot{\alpha}_{3\,(b_3)} = \dot{\alpha}_3 \end{cases} \tag{31}$$

Thus, the angular velocity expressed in the body-fixed coordinate system **ω** has the following relationship with the derivatives of the Euler angles by summing above equations.

$$\begin{cases} \omega_{(b_1)} = \dot{\alpha}_1 \cos\alpha_3 \cdot \cos\alpha_2 + \dot{\alpha}_2 \sin\alpha_3 \\ \omega_{(b_2)} = \dot{\alpha}_1 \cos\alpha_2 \cdot (-\sin\alpha_3) + \dot{\alpha}_2 \cos\alpha_3 \\ \omega_{(b_3)} = \dot{\alpha}_1 \sin\alpha_2 + \dot{\alpha}_3 \end{cases} \tag{32}$$

The relationship can be expressed in the matrix form of

$$\boldsymbol{\omega} = \mathbf{B}\frac{d\boldsymbol{\alpha}}{dt} \tag{33}$$

where, the transfer matrix of angular velocity **B** is

$$\mathbf{B} = \begin{bmatrix} \cos\alpha_3 \cos\alpha_2 & \sin\alpha_3 & 0 \\ -\sin\alpha_3 \cos\alpha_2 & \cos\alpha_3 & 0 \\ \sin\alpha_2 & 0 & 1 \end{bmatrix} \tag{34}$$

APPENDIX B

DERIVATIONS OF THE PENDULUM MODEL

This section presents the derivation of the 4-DOF (x, z, θ, and α) motion equation of the pendulum by the Lagrange's Equation in detail.

Using the defined coordinates of point G and P by Eq. 5 in text, the velocity of each pendulum (or wheel) is calculated.

$$\begin{aligned} v_1 &= \left(\dot{x},\ \dot{z}\right) \\ v_2 &= \left(\dot{x} - d\dot{\theta}\cos\theta - l\left(\dot{\theta}+\dot{\alpha}\right)\cos\left(\theta+\alpha\right),\ \dot{z} + d\dot{\theta}\sin\theta + l\left(\dot{\theta}+\dot{\alpha}\right)\sin\left(\theta+\alpha\right)\right) \end{aligned} \tag{35}$$

where, v_1 is the velocity of the pendulum wheel G and v_2 is the velocity of the pendulum P.

The kinetic energy K and potential energy P of each pendulum are calculated as below, and the Lagrangian L is defined by them as shown in Eq. 6.

$$K_1 = \frac{1}{2} I_1 \dot{\theta}^2 + \frac{1}{2} m_1 v_1^2 = \frac{1}{2} I_1 \dot{\theta}^2 + \frac{1}{2} m_1 \left(\dot{x}^2 + \dot{z}^2\right) \tag{36}$$

$$\begin{aligned} & K_2 \\ &= \frac{1}{2} I_2 \left(\dot{\theta}+\dot{\alpha}\right)^2 + \frac{1}{2} m_2 v_2^2 \\ &= \frac{1}{2} I_2 \left(\dot{\theta}+\dot{\alpha}\right)^2 + \frac{1}{2} m_2 \left[\begin{array}{l} \left\{\dot{x} - d\dot{\theta}\cos\theta - l\left(\dot{\theta}+\dot{\alpha}\right)\cos\left(\theta+\alpha\right)\right\}^2 + \\ \left\{\dot{z} + d\dot{\theta}\sin\theta + l\left(\dot{\theta}+\dot{\alpha}\right)\sin\left(\theta+\alpha\right)\right\}^2 \end{array}\right] \\ &= \frac{1}{2} I_2 \left(\dot{\theta}+\dot{\alpha}\right)^2 + \frac{1}{2} m_2 \left[\begin{array}{l} \dot{x}^2 + \dot{z}^2 + d^2\dot{\theta}^2 + l^2\left(\dot{\theta}+\dot{\alpha}\right)^2 + \\ 2\left\{\begin{array}{l} -d\,\dot{x}\,\dot{\theta}\cos\theta + d\,\dot{z}\,\dot{\theta}\sin\theta - l\,\dot{x}\left(\dot{\theta}+\dot{\alpha}\right)\cos\left(\theta+\alpha\right) + \\ l\,\dot{z}\left(\dot{\theta}+\dot{\alpha}\right)\sin\left(\theta+\alpha\right) + d\,l\,\dot{\theta}\left(\dot{\theta}+\dot{\alpha}\right)\cos\alpha \end{array}\right\} \end{array}\right] \end{aligned} \tag{37}$$

$$P_1 = m_1 g z \tag{38}$$

$$P_2 = m_2 g \left\{ z - d\cos\theta - l\cos\left(\theta + \alpha\right) \right\} \tag{39}$$

Eq. 4 derives a set of motion equations for each generalized variable x, z, θ, and α.

The derivative of L with respect to the generalized variable x:

$$\frac{\partial L}{\partial \dot{x}} = \left(m_1 + m_2\right)\dot{x} - m_2 d\dot{\theta}\cos\theta - m_2 l\left(\dot{\theta} + \dot{\alpha}\right)\cos\left(\theta + \alpha\right) \tag{40}$$

$$\frac{\partial L}{\partial x} = 0 \tag{41}$$

Thus, the first row of the equation by the Lagrange's Equation is

$$\begin{aligned} &\left(m_1 + m_2\right)\ddot{x} - m_2 d\left(\ddot{\theta}\cos\theta - \dot{\theta}^2\sin\theta\right) \\ &-m_2 l\left\{\left(\ddot{\theta} + \ddot{\alpha}\right)\cos\left(\theta + \alpha\right) - \left(\dot{\theta} + \dot{\alpha}\right)^2\sin\left(\theta + \alpha\right)\right\} = 0 \end{aligned} \tag{42}$$

The derivative of L with respect to the generalized variable z:

$$\frac{\partial L}{\partial \dot{z}} = \left(m_1 + m_2\right)\dot{z} + m_2 d\dot{\theta}\sin\theta + m_2 l\left(\dot{\theta} + \dot{\alpha}\right)\sin\left(\theta + \alpha\right) \tag{43}$$

$$\frac{\partial L}{\partial z} = -\left(m_1 + m_2\right)g \tag{44}$$

Thus, the second row of the motion equation by the Lagrange's Equation is

$$\begin{aligned} &\left(m_1 + m_2\right)\ddot{z} + m_2 d\left(\ddot{\theta}\sin\theta + \dot{\theta}^2\cos\theta\right) \\ &\quad + m_2 l\left\{\left(\ddot{\theta} + \ddot{\alpha}\right)\sin\left(\theta + \alpha\right) + \left(\dot{\theta} + \dot{\alpha}\right)^2\cos\left(\theta + \alpha\right)\right\} + \left(m_1 + m_2\right)g = 0 \end{aligned} \tag{45}$$

The derivative of L with respect to the generalized variable θ:

$$\frac{\partial L}{\partial \dot{\theta}} = (I_1 + I_2)\dot{\theta} + I_2\dot{\alpha} + m_2 d^2\dot{\theta} + m_2 l^2(\dot{\theta} + \dot{\alpha}) - m_2 d\,\dot{x}\cos\theta + m_2 d\,\dot{z}\sin\theta - m_2 l\,\dot{x}\cos(\theta + \alpha) + m_2 l\,\dot{z}\sin(\theta + \alpha) + m_2 d\,l(2\dot{\theta} + \dot{\alpha})\cos\alpha \tag{46}$$

$$\frac{\partial L}{\partial \theta} = m_2 d\,\dot{x}\,\dot{\theta}\sin\theta + m_2 d\,\dot{z}\dot{\theta}\cos\theta + m_2 l\,\dot{x}(\dot{\theta} + \dot{\alpha})\sin(\theta + \alpha) + m_2 l\,\dot{z}(\dot{\theta} + \dot{\alpha})\cos(\theta + \alpha) - m_2 g\{d\sin\theta + l\sin(\theta + \alpha)\} \tag{47}$$

Thus, the third row of the motion equation by the Lagrange's Equation is

$$-m_2 d\,\ddot{x}\cos\theta + m_2 d\,\ddot{z}\sin\theta - m_2 l\,\ddot{x}\cos(\theta + \alpha) + m_2 l\,\ddot{z}\sin(\theta + \alpha) + (I_1 + I_2 + m_2 d^2 + m_2 l^2)\ddot{\theta} + (I_2 + m_2 l^2)\ddot{\alpha} + m_2 d\,l(2\ddot{\theta} + \ddot{\alpha})\cos\alpha - m_2 d\,l(2\dot{\theta}\dot{\alpha} + \dot{\alpha}^2)\sin\alpha + m_2 g\{d\sin\theta + l\sin(\theta + \alpha)\} = 0 \tag{48}$$

The derivative of L with respect to the generalized variable α:

$$\frac{\partial L}{\partial \dot{\alpha}} = I_2(\dot{\theta} + \dot{\alpha}) - m_2\,l\,\dot{x}\cos(\theta + \alpha) + m_2\,l\,\dot{z}\sin(\theta + \alpha) + m_2 l^2(\dot{\theta} + \dot{\alpha}) + m_2 d\,l\,\dot{\theta}\cos\alpha \tag{49}$$

$$\frac{\partial L}{\partial \alpha} = m_2 l\,\dot{x}(\dot{\theta} + \dot{\alpha})\sin(\theta + \alpha) + m_2 l\,\dot{z}(\dot{\theta} + \dot{\alpha})\cos(\theta + \alpha) - m_2\,d\,l\,\dot{\theta}(\dot{\theta} + \dot{\alpha})\sin\alpha - m_2 g l\sin(\theta + \alpha) \tag{50}$$

Thus, the fourth row of the motion equation by the Lagrange's Equation is

$$-m_2\,l\,\ddot{x}\cos(\theta + \alpha) + m_2\,l\,\ddot{z}\sin(\theta + \alpha) + (I_2 + m_2 l^2 + m_2\,d\,l\cos\alpha)\ddot{\theta} + (I_2 + m_2 l^2)\ddot{\alpha} + m_2\,d\,l\,\dot{\theta}^2\sin\alpha + m_2 g l\sin(\theta + \alpha) = 0 \tag{51}$$

These equations are formulated in the matrix form of Eq. 7 using Eqs. 8-10 in text.

The system of linearized motion equations for $X=(x, z, \theta, \alpha)^T$ is below. In this case, the linearization makes F_p in Eq. 10 divided into a linear term KX and a

conservative force F, which is the gravitational force. The details can also be found in the previous study (Babarit, 2005). Note that the final form in this appendix remains θ and α in the second row and column by linearizing sin θ, sin α, and sin $(\theta+\alpha)$ to θ, α, and $\theta+\alpha$ respectively, whereas the earlier study neglected the related terms in the final form.

$$M\ddot{X} + KX = F \tag{52}$$

$$M = \begin{pmatrix} m_1 + m_2 & 0 & -m_2 d - m_2 l & -m_2 l \\ 0 & m_1 + m_2 & m_2 (d+l)\theta + m_2 l\alpha & m_2 l(\theta+\alpha) \\ -m_2 d - m_2 l & m_2 (d+l)\theta + m_2 l\alpha & I_1 + I_2 + m_2 d^2 + m_2 l^2 + 2m_2 dl & I_2 + m_2 l^2 + m_2 dl \\ -m_2 l & m_2 l(\theta+\alpha) & I_2 + m_2 l^2 + m_2 dl & I_2 + m_2 l^2 \end{pmatrix}, \tag{53}$$

$$K = \begin{pmatrix} 0 & 0 & 0 & 0 \\ 0 & 0 & 0 & 0 \\ 0 & 0 & m_2 g(d+l) & m_2 g l \\ 0 & 0 & m_2 g l & m_2 g l \end{pmatrix}, \tag{54}$$

$$F = \begin{pmatrix} 0 \\ -(m_1 + m_2) g \\ 0 \\ 0 \end{pmatrix}. \tag{55}$$

APPENDIX C

THICKNESS OF THE PENDULUM WHEEL

There are many ways to design an inner pendulum wheel as previous studies sketched or designed (Ruellan et al., 2007; Ruellan et al., 2010). Use of a solid homogeneous fan-shape body is the simplest way to design an inner pendulum, whose gravitational center is set off from a pivot point.

The centroid of a fan-shape body is as below.

$$c = \frac{4r\sin(\beta/2)}{3\beta} \tag{56}$$

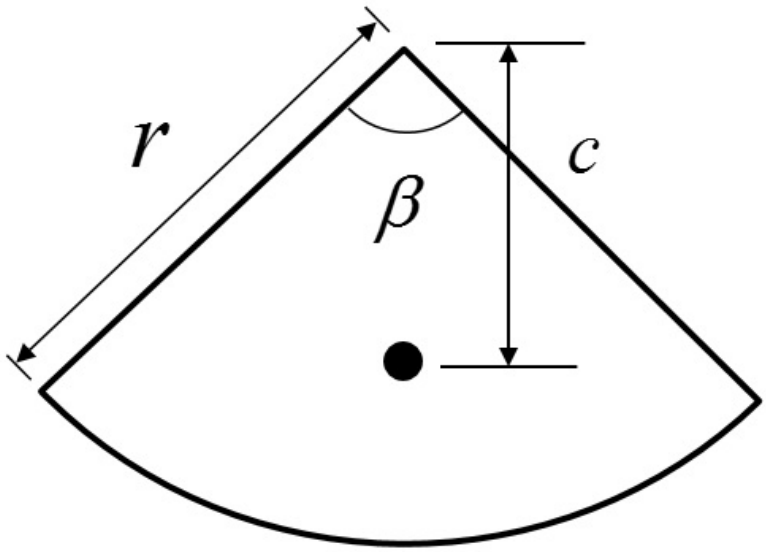

Figure 33 Centroid of fan-shape body

The thickness of the fan-shape is very sensitive to the angle β to keep a mass quantity constant as shown Fig. 32. In the figure, the thickness ratio defines the ratio of a thickness for a circular body to a thickness for a fan-shape body, whose radius and mass are same as the circular body. Considering the limited space inside of the oceanographic buoy and practical material (e.g. concrete), c/r is recommended to be set below 0.55 to 0.60.

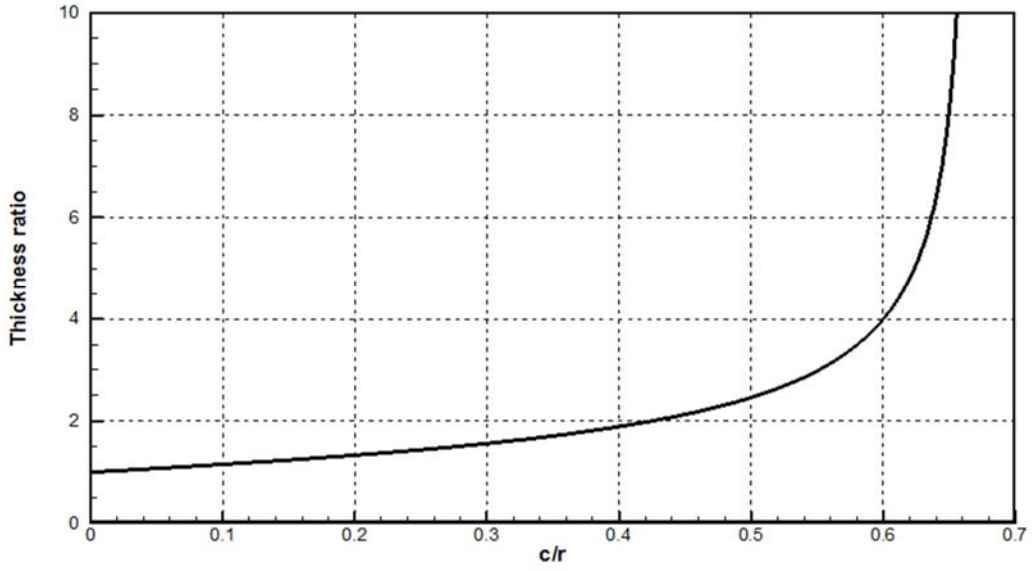

Figure 34 Thickness ratio of fan-shape body

APPENDIX D

COUPLE SIMULATION RESULTS

This section plots the results of surge and pitch motions among 6-DOF motions calculated by COUPLE for nine wave conditions. The surge and pitch motions for each wave condition are attached on a separate page.

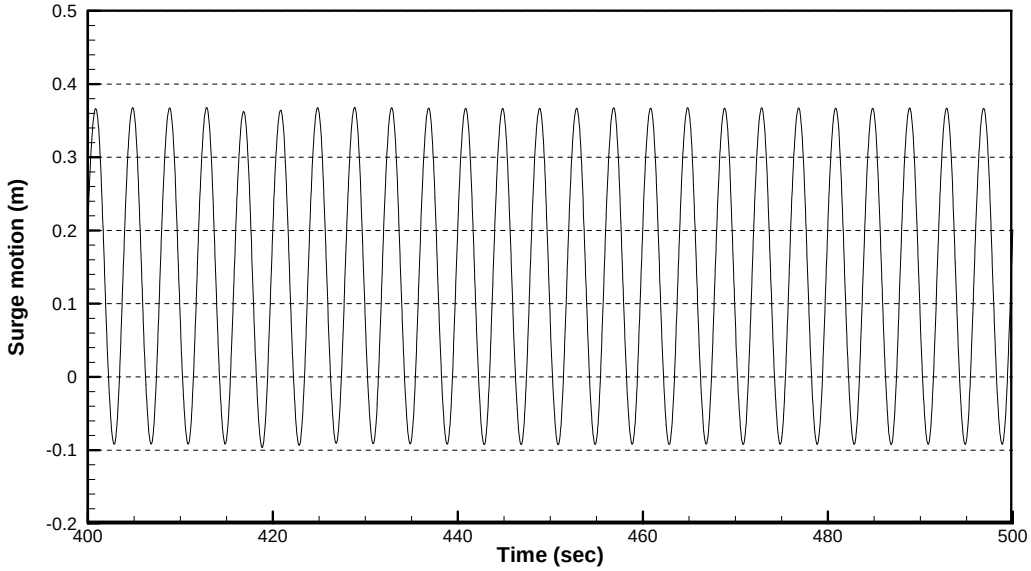

Figure 35 Surge motion for regular waves (H=0.5 m, T=4.0 sec)

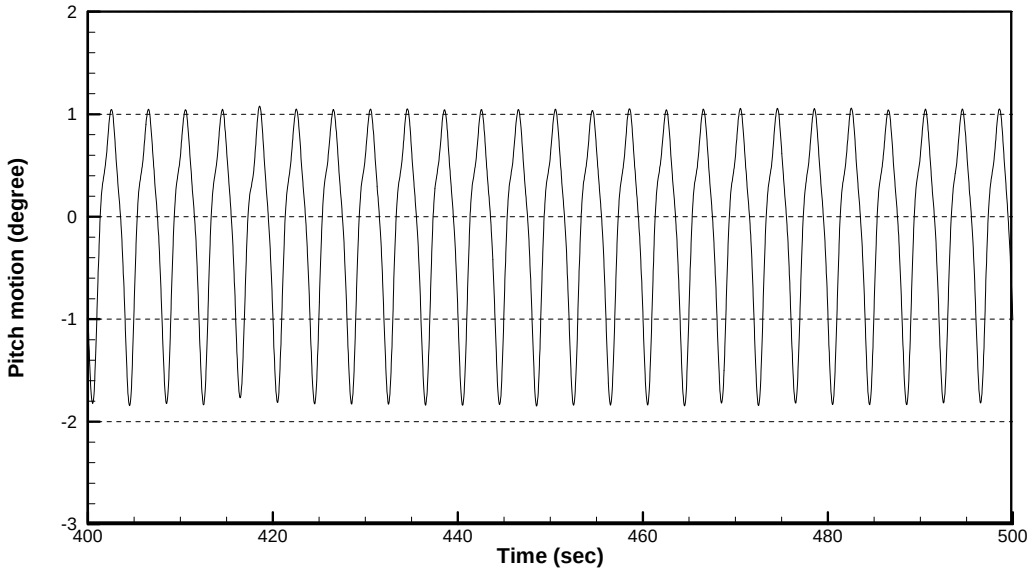

Figure 36 Pitch motion for regular waves (H=0.5 m, T=4.0 sec)

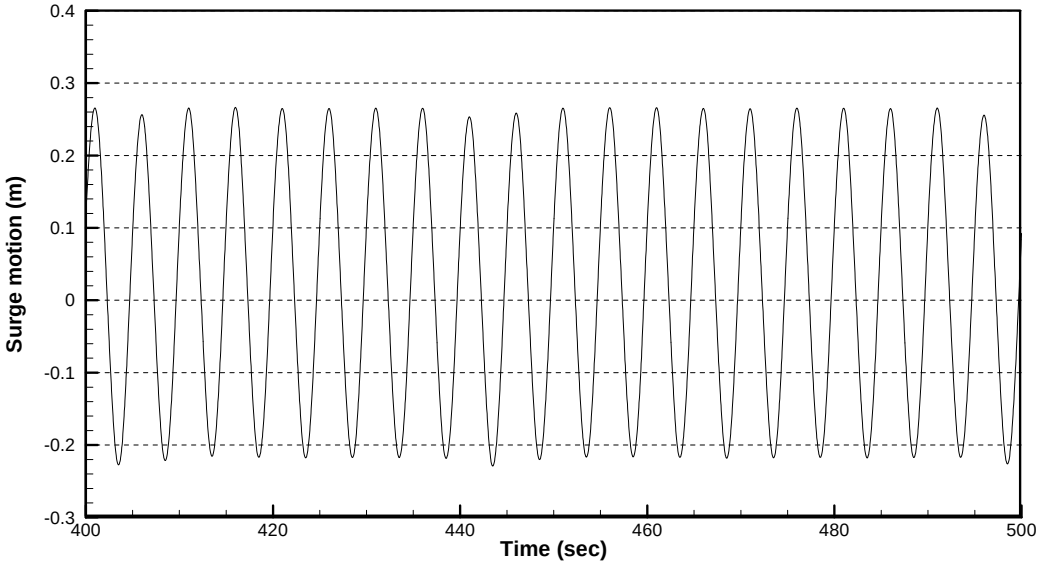

Figure 37 Surge motion for regular waves (H=0.5 m, T=5.0 sec)

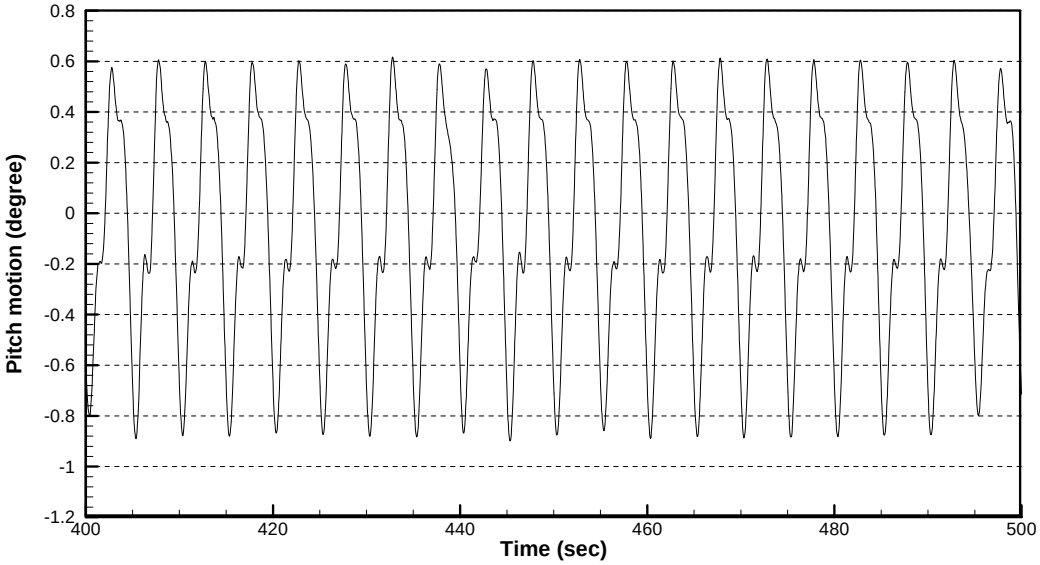

Figure 38 Pitch motion for regular waves (H=0.5 m, T=5.0 sec)

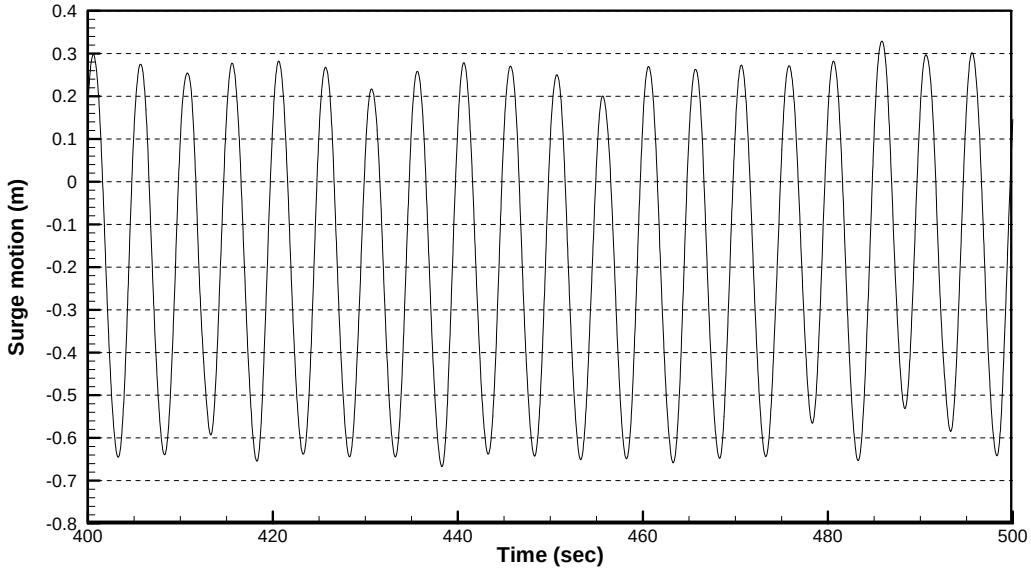

Figure 39 Surge motion for regular waves (H=1.0 m, T=5.0 sec)

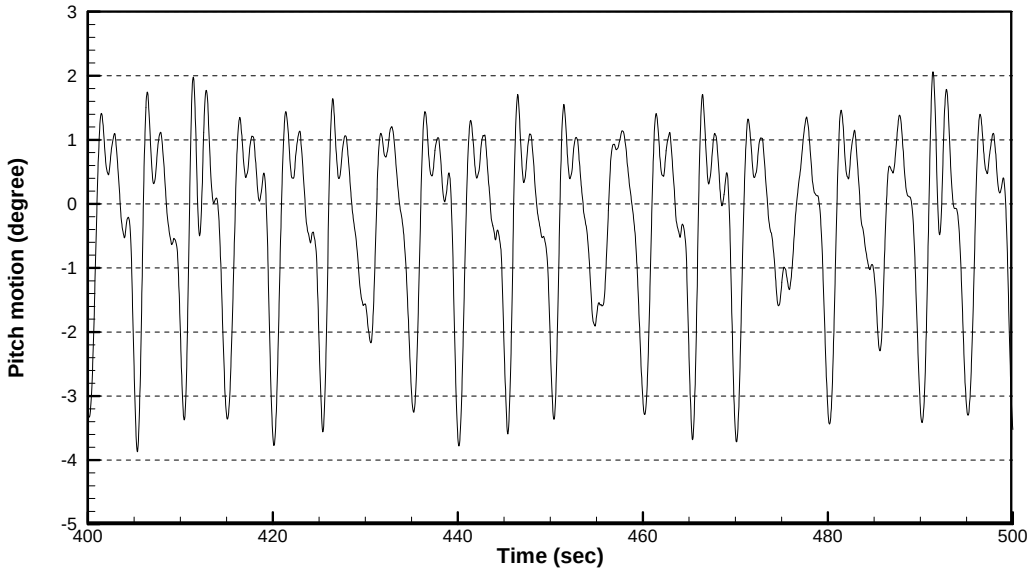

Figure 40 Pitch motion for regular waves (H=1.0 m, T=5.0 sec)

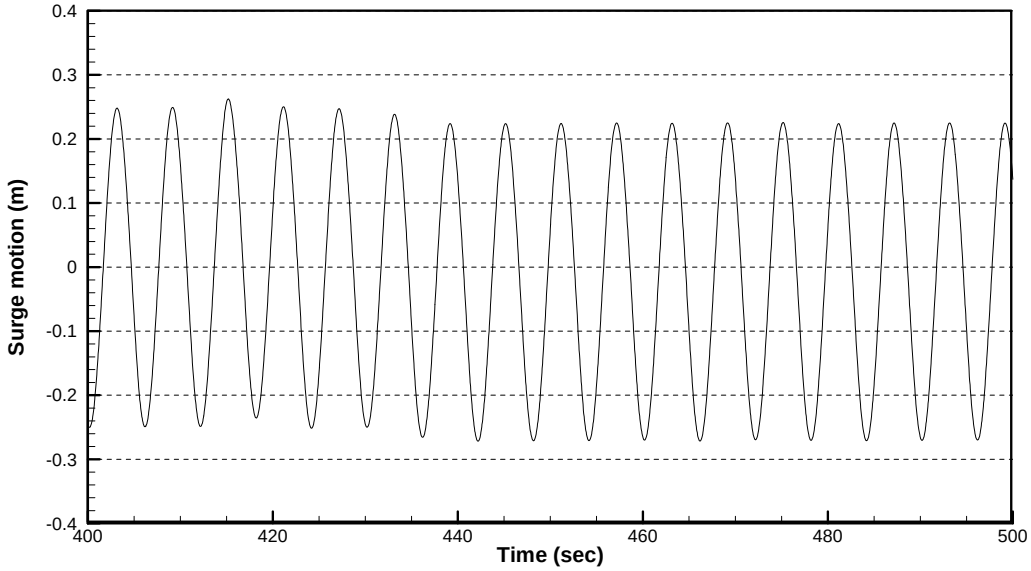

Figure 41 Surge motion for regular waves (H=0.5 m, T=6.0 sec)

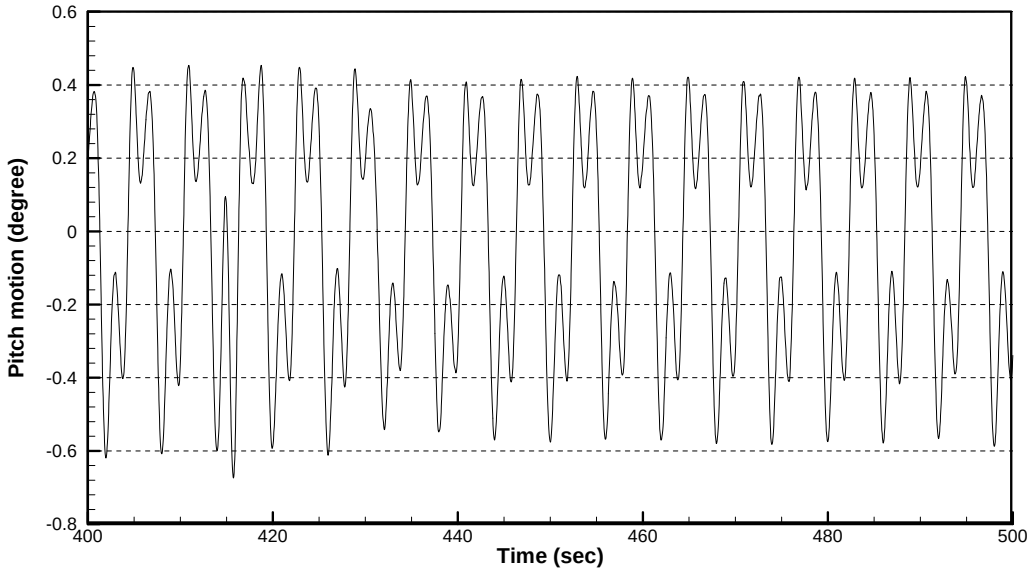

Figure 42 Pitch motion for regular waves (H=0.5 m, T=6.0 sec)

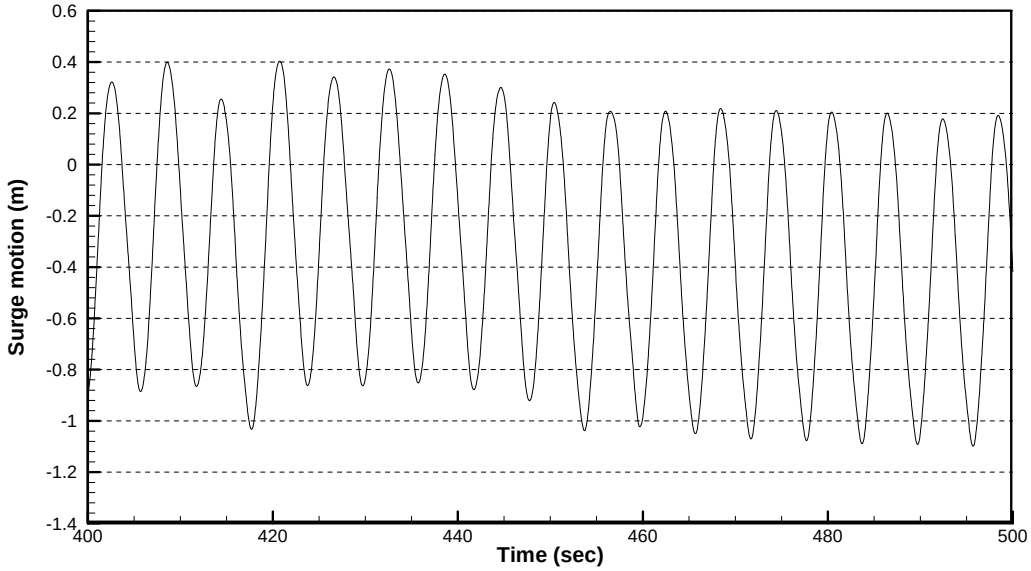

Figure 43 Surge motion for regular waves (H=1.5 m, T=6.0 sec)

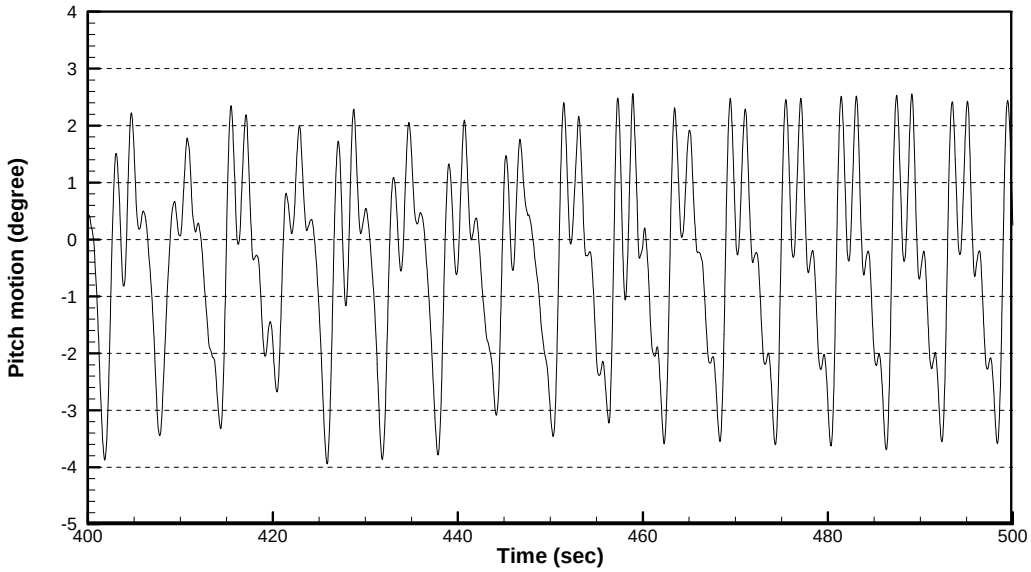

Figure 44 Pitch motion for regular waves (H=1.5 m, T=6.0 sec)

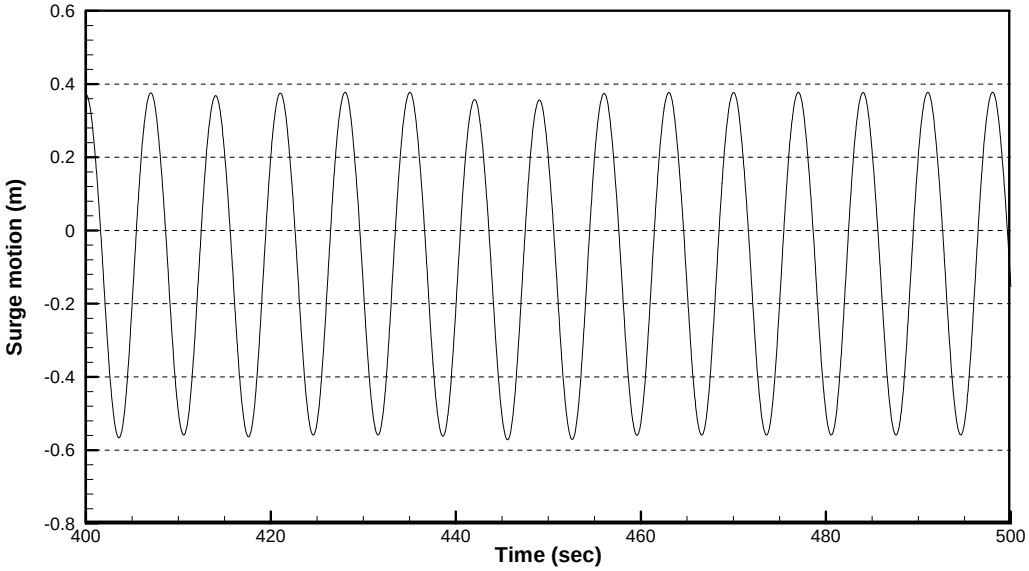

Figure 45 Surge motion for regular waves (H=1.0 m, T=7.0 sec)

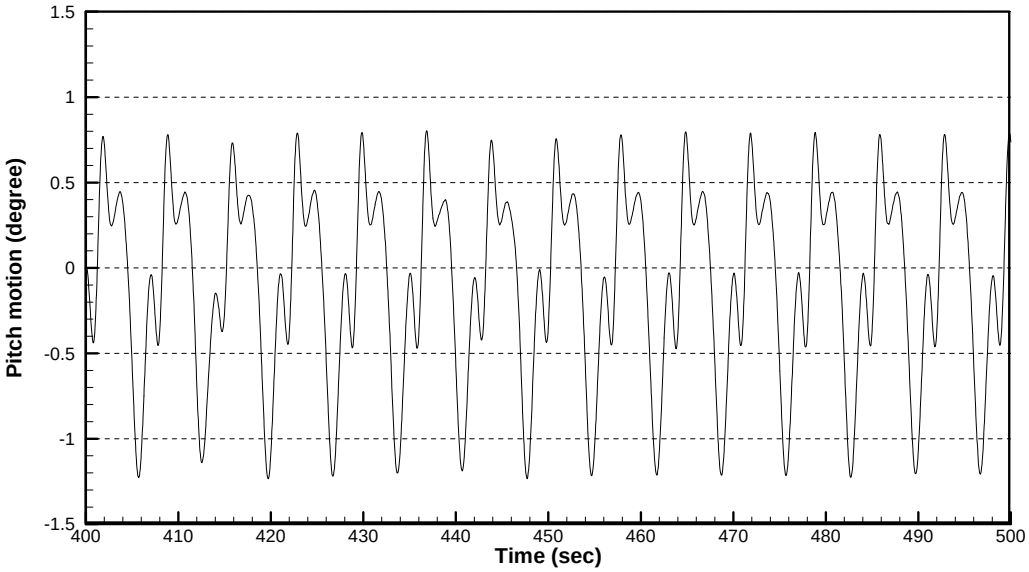

Figure 46 Pitch motion for regular waves (H=1.0 m, T=7.0 sec)

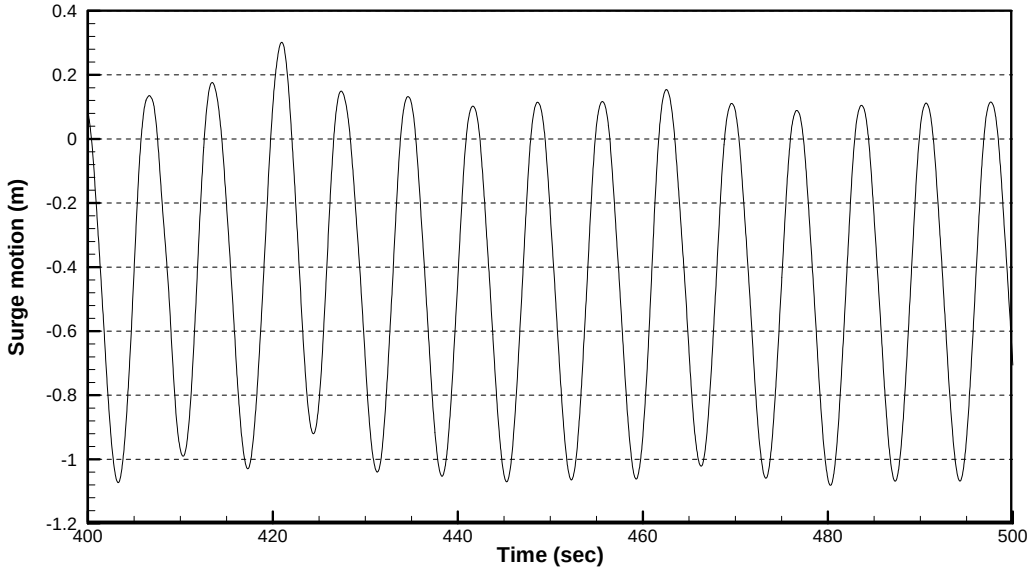

Figure 47 Surge motion for regular waves (H=1.5 m, T=7.0 sec)

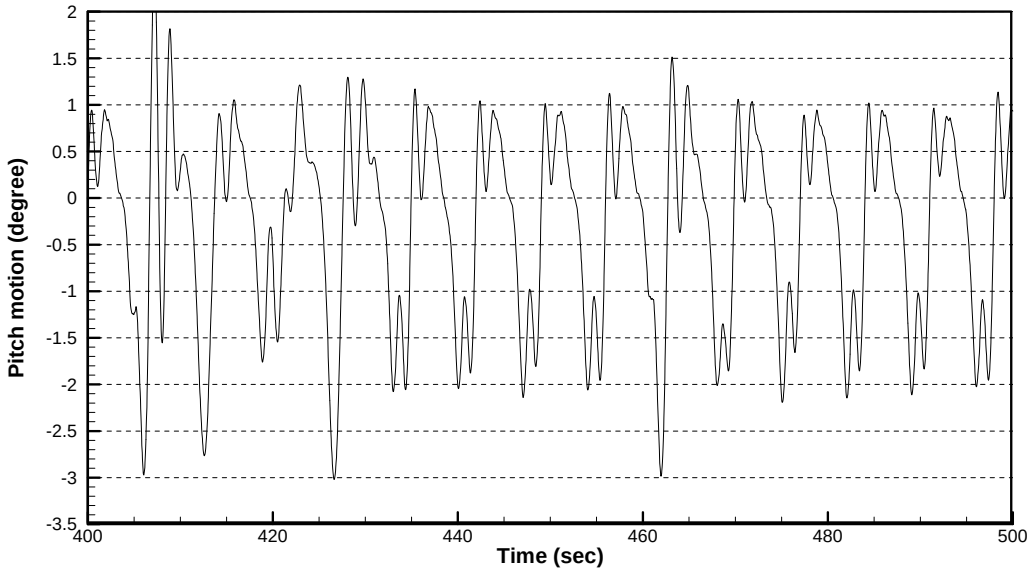

Figure 48 Pitch motion for regular waves (H=1.5 m, T=7.0 sec)

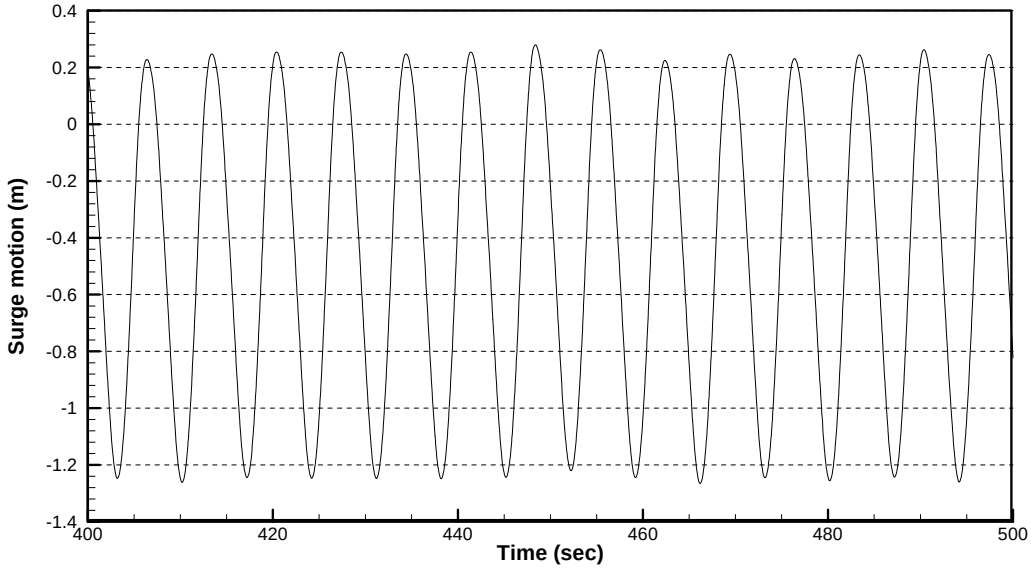

Figure 49 Surge motion for regular waves (H=2.0 m, T=7.0 sec)

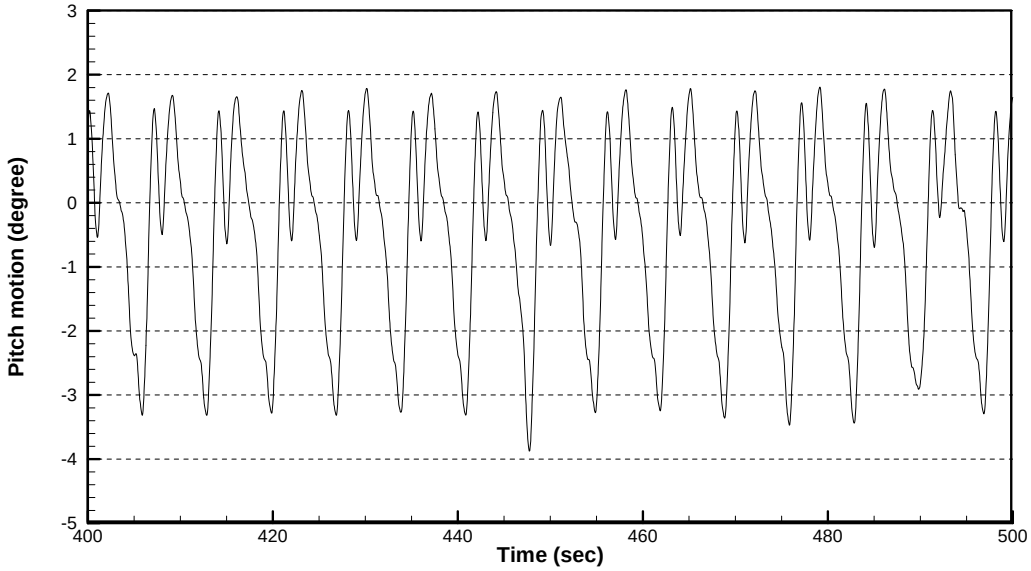

Figure 50 Pitch motion for regular waves (H=2.0 m, T=7.0 sec)

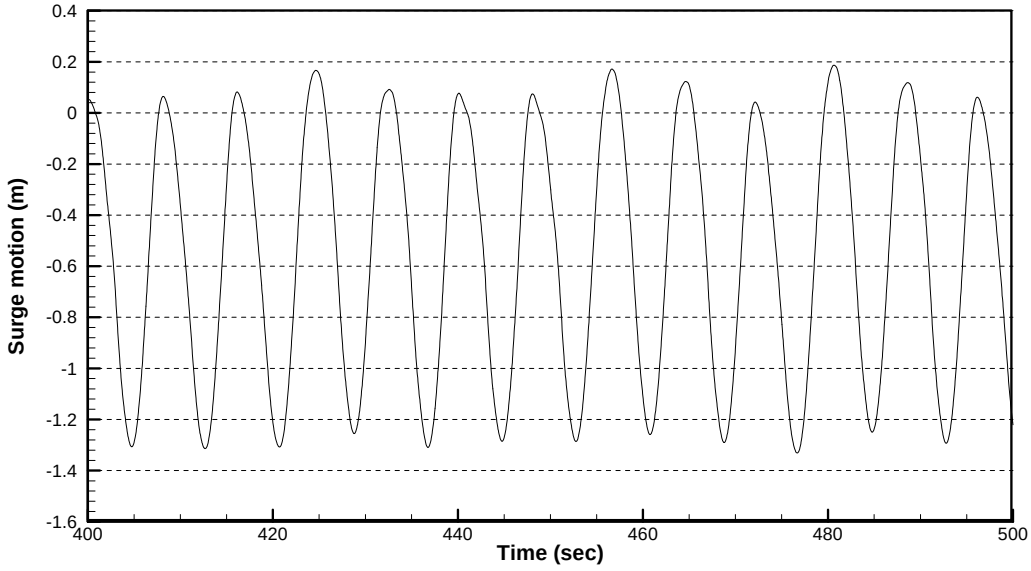

Figure 51 Surge motion for regular waves (H=2.0 m, T=8.0 sec)

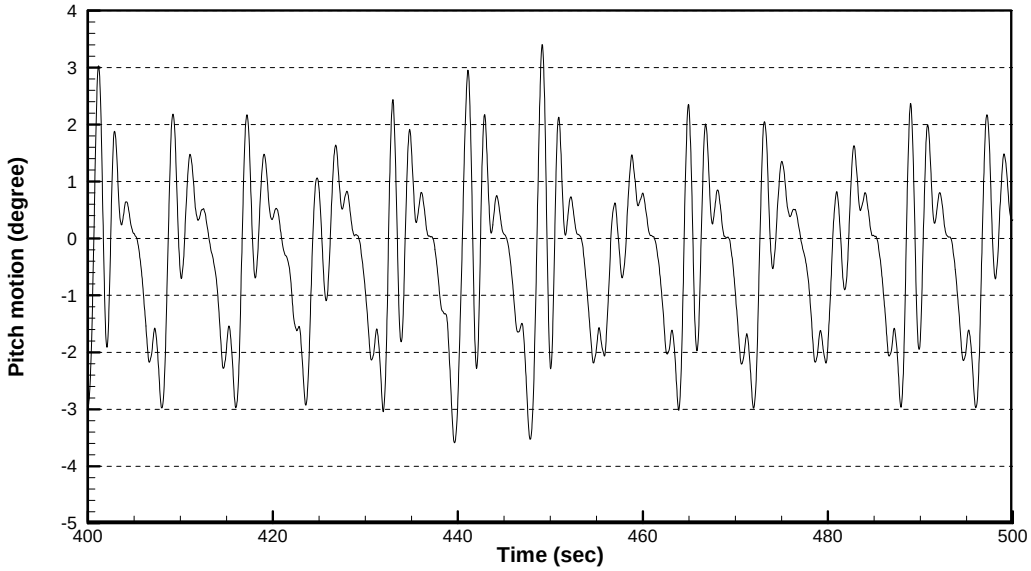

Figure 52 Pitch motion for regular waves (H=2.0 m, T=8.0 sec)